

**Special Section:**ExoMars Trace Gas Orbiter -  
One Martian Year of Science**Key Points:**

- We assimilate temperature and dust observations from ExoMars Trace Gas Orbiter-Atmospheric Chemistry Suite-TIRVIM during the MY34 global dust storm (GDS)
- The analysis verifies well against independent Mars Climate Sounder temperature and dust profiles, and Curiosity pressure measurements
- At the peak of the GDS the winds strengthen, the diurnal tide migrates poleward, and the semi-diurnal tide strengthens

**Supporting Information:**

Supporting Information may be found in the online version of this article.

**Correspondence to:**R. M. B. Young,  
[roland.young@uaeu.ac.ae](mailto:roland.young@uaeu.ac.ae)**Citation:**

Young, R. M. B., Millour, E., Guerlet, S., Forget, F., Ignatiev, N., Grigoriev, A. V., et al. (2022). Assimilation of temperatures and column dust opacities measured by ExoMars TGO-ACS-TIRVIM during the MY34 global dust storm. *Journal of Geophysical Research: Planets*, 127, e2022JE007312. <https://doi.org/10.1029/2022JE007312>

Received 21 APR 2022








Accepted 22 AUG 2022

**Author Contributions:****Conceptualization:** Roland M. B. Young, Ehouarn Millour, François Forget**Data curation:** Ehouarn Millour, Nikolay Ignatiev**Formal analysis:** Roland M. B. Young**Funding acquisition:** François Forget, Franck Montmessin, Oleg Korablev

© 2022. The Authors.

This is an open access article under the terms of the [Creative Commons Attribution-NonCommercial License](https://creativecommons.org/licenses/by-nc/4.0/), which permits use, distribution and reproduction in any medium, provided the original work is properly cited and is not used for commercial purposes.

## Assimilation of Temperatures and Column Dust Opacities Measured by ExoMars TGO-ACS-TIRVIM During the MY34 Global Dust Storm

Roland M. B. Young<sup>1,2</sup> , Ehouarn Millour<sup>2</sup> , Sandrine Guerlet<sup>2,3</sup> , François Forget<sup>2</sup>, Nikolay Ignatiev<sup>4</sup>, Alexey V. Grigoriev<sup>4</sup>, Alexey V. Shakun<sup>4</sup> , Alexander Trokhimovskiy<sup>4</sup> , Franck Montmessin<sup>5</sup> , and Oleg Korablev<sup>4</sup> 

<sup>1</sup>Department of Physics, National Space Science and Technology Center, United Arab Emirates University, Al Ain, UAE,<sup>2</sup>Laboratoire de Météorologie Dynamique (LMD/IPSL), Sorbonne Université, ENS, PSL Research University, École Polytechnique, Institut Polytechnique de Paris, CNRS, Paris, France, <sup>3</sup>LESIA, Observatoire de Paris, Université PSL, CNRS, Sorbonne Université, Université de Paris, Meudon, France, <sup>4</sup>Space Research Institute (IKI), Moscow, Russia, <sup>5</sup>LATMOS/IPSL, UVSQ Université Paris-Saclay, UPMC Univ. Paris 06, CNRS, Guyancourt, France

**Abstract** We assimilate atmospheric temperature profiles and column dust optical depth observations from the ExoMars Trace Gas Orbiter Atmospheric Chemistry Suite thermal infrared channel (TIRVIM) into the Mars Planetary Climate Model. The assimilation period is Mars Year 34  $L_s = 182.3^\circ$ – $211.4^\circ$ , covering the onset and peak of the 2018 global dust storm. We assimilated observations using the Local Ensemble Transform Kalman Filter with 36 ensemble members and adaptive inflation; our nominal configuration assimilated TIRVIM temperature profiles to update temperature and dust profiles, followed by dust column optical depths to update the total column dust abundance. The observation operator for temperature used the averaging kernels and prior profile from the TIRVIM retrievals. We verified our analyses against in-sample TIRVIM observations and independent Mars Climate Sounder (MCS) temperature and dust density-scaled opacity profiles. When dust observations were assimilated, the root-mean-square temperature error verified against MCS fell by 50% during the onset period of the storm, compared with assimilating temperature alone. At the peak of the storm the analysis reproduced the location and magnitude of the peak in the nighttime MCS dust distribution, along with the surface pressure diurnal cycle measured by Curiosity with a bias of less than 10 Pa. The analysis winds showed that, at the peak of the storm, the meridional circulation strengthened, a  $125 \text{ m s}^{-1}$  asymmetry developed in the midlatitude zonal jets, the diurnal tide weakened near the equator and strengthened to 10–15 K at midlatitudes, and the semi-diurnal tide strengthened almost everywhere, particularly in the equatorial lower atmosphere.

**Plain Language Summary** ExoMars Trace Gas Orbiter has been in low orbit around Mars since early 2018. During 2018 a large amount of dust was lifted from Mars' surface into the atmosphere. This eventually obscured most of the planet, forming a global dust storm. These storms have a large effect on the temperature and weather in Mars' atmosphere. We used observations from the spacecraft's thermal infrared instrument. This measures how much light comes from the atmosphere and surface at wavelengths where heat is emitted, and can be used to work out the atmospheric temperature and dust content at different times of day. We combined these observations with a numerical model of Mars' atmosphere, considering uncertainties in the measured atmospheric properties and the modeled atmosphere. We compared our results with temperature and dust observations made by Mars Climate Sounder on board Mars Reconnaissance Orbiter. Including dust observations was better than just using temperature observations. While the dust storm was raging, north-south wind speeds increased, the strong eastward wind in the northern hemisphere became much stronger than in the southern hemisphere, and differences between day and night became larger. Our results mean we can better understand aspects of Mars' atmosphere throughout the daily cycle.

### 1. Introduction

The ExoMars Trace Gas Orbiter (TGO) reached its final orbit around Mars in April 2018. It carries the Atmospheric Chemistry Suite (ACS), which comprises three infrared spectrometers covering different wavelength ranges (Korablev et al., 2018). The thermal infrared spectrometer TIRVIM was designed to continuously monitor the atmospheric column in nadir, while the near- and mid-infrared channels NIR and MIR (and occasionally

**Investigation:** Roland M. B. Young, Ehouarn Millour, Sandrine Guerlet, François Forget, Nikolay Ignatiev, Alexey V. Grigoriev, Alexey V. Shakun, Alexander Trokhimovskiy, Franck Montmessin, Oleg Korablev  
**Methodology:** Roland M. B. Young, Ehouarn Millour, Sandrine Guerlet, François Forget  
**Project Administration:** Ehouarn Millour, François Forget, Alexander Trokhimovskiy, Franck Montmessin, Oleg Korablev  
**Resources:** Nikolay Ignatiev, Alexey V. Grigoriev, Alexey V. Shakun, Alexander Trokhimovskiy, Franck Montmessin, Oleg Korablev  
**Software:** Roland M. B. Young, Ehouarn Millour, Sandrine Guerlet, François Forget  
**Supervision:** Ehouarn Millour, François Forget  
**Validation:** Roland M. B. Young  
**Visualization:** Roland M. B. Young  
**Writing – original draft:** Roland M. B. Young  
**Writing – review & editing:** Roland M. B. Young, Ehouarn Millour, Sandrine Guerlet, François Forget

TIRVIM) perform solar occultation measurements when the spacecraft-Mars-Sun geometry permits. TGO's orbit made ACS-TIRVIM's (TIRVIM hereafter) observations of Mars unique at the time among existing Mars spacecraft, because it systematically measured the atmospheric structure over all local times of day. Nearly all spacecraft that have orbited Mars since Mars Global Surveyor at the start of the modern era have taken observations at two fixed local times of day separated by 12 hr (Mars Express has an orbit that means it does take observations at varying local times of day (Giuranna et al., 2021), but not systematically, and since May 2021 the Emirates Mars Mission has observed Mars from high orbit with full local time coverage (Amiri et al., 2022)). TGO takes about 55 sols to cycle through the full 24 hr of sub-spacecraft local times, which is close to the optimal repeat period to sample the diurnal cycle (Capderou & Forget, 2004).

TIRVIM took observations at Mars from March 2018, shortly before TGO reached its final orbit, until the end of 2019, when its cryocooler failed, rendering it impossible to cool the instrument to the required temperature to make thermal infrared measurements. At the start of this ~20-month period, about halfway through Mars Year (MY) 34, a global dust storm (GDS) took place. This started around  $L_s = 186^\circ$  in Acidalia, reached a peak in visible dust optical depth between  $L_s = 200\text{--}205^\circ$ , and faded away by about  $L_s = 300^\circ$  (Kass et al., 2019; Kleinböhl et al., 2020; Montabone et al., 2020). The storm was severe enough to end the solar-powered Opportunity rover's 15-year mission. The start of the TIRVIM data set covers the onset and peak of this GDS; fortuitously, as these events happen in only about 1 MY out of three (Kahre et al., 2017).

Over the last 20–25 years, scientists have studied Mars using data assimilation, which combines observations with our best scientific understanding encoded within numerical simulations (Kalnay, 2003). A variety of methods have been used, with most work using Analysis Correction (AC; Lewis & Read, 1995; Lewis et al., 2007; Lorenc et al., 1991; Steele, Lewis, & Patel, 2014) or the Ensemble Kalman Filter (EnKF; Evensen, 2003; Greybush et al., 2012; M. J. Hoffman et al., 2010; Navarro et al., 2014). These have assimilated various observations, primarily atmospheric temperature profiles, but also dust column optical depths (Lewis & Barker, 2005; Montabone et al., 2014; Ruan et al., 2021), dust profiles (Navarro et al., 2017; Ruan et al., 2021), and column abundances of water ice (Steele, Lewis, & Patel, 2014), water vapor (Steele, Lewis, Patel, Montmessin, et al., 2014), ozone (Holmes et al., 2018), and carbon monoxide (Holmes et al., 2019). The primary assimilated quantity is temperature, because it is readily available from thermal infrared measurements from multiple spacecraft, changes in other atmospheric quantities such as pressure and winds are related to changes in temperature via known physical laws, and while wind observations are a vital part of Earth data assimilation (Hersbach et al., 2019), they are not available for Mars.

Most relevant to the current work, Navarro et al. (2014, 2017) built a data assimilation scheme for Mars' atmosphere using the Local Ensemble Transform Kalman Filter (LETKF; Hunt et al., 2007) and the Mars Planetary Climate Model (Mars PCM), a Global Climate Model (GCM) formerly called the Laboratoire de Météorologie Dynamique Mars Global Climate Model (LMD Mars GCM) (Forget et al., 1999; Francois et al., 2022; Pottier et al., 2017). They assimilated observations from the Mars Climate Sounder (MCS) instrument on board NASA's Mars Reconnaissance Orbiter. MCS retrieval products include temperature, dust, and water ice profiles taken from a Sun-synchronous polar orbit at ~3 a.m./3 p.m. local mean solar time (Kleinböhl et al., 2009).

In this paper we report on assimilation of observations from the early part of the ExoMars TGO ACS-TIRVIM observation period, covering the onset and peak of the MY34 GDS. We make two methodological improvements to the existing scheme documented by Navarro et al. (2017). First, we improve the way temperature forecasts are compared with observations by using the averaging kernel matrix and prior from the TIRVIM temperature retrievals. This is the correct way to compare forecast with observations when assimilating retrieval products (R. N. Hoffman, 2011). Second, the scheme can now assimilate column dust optical depths (CDODs); previous work with this particular scheme did not assimilate CDOD because such data are not available from MCS (while dust profiles are available, they do not reach the ground, and published MCS CDODs interpolate the dust profiles to the ground in the lowest part of the atmosphere, typically the lowest 10 km). We describe both of these improvements in detail in Section 3.

The aims of this paper are as follows. First, to demonstrate assimilation of observations from TIRVIM on board ExoMars TGO. Second, to validate the assimilation against independent data sets such as MCS temperatures and dust opacities, and surface pressure measurements from the Curiosity rover. Finally, to investigate the dynamics of Mars' atmosphere during the MY34 GDS, particularly those properties that cannot be measured directly but which can be retrieved by the assimilation process, such as wind. Section 2 describes the TIRVIM observations,

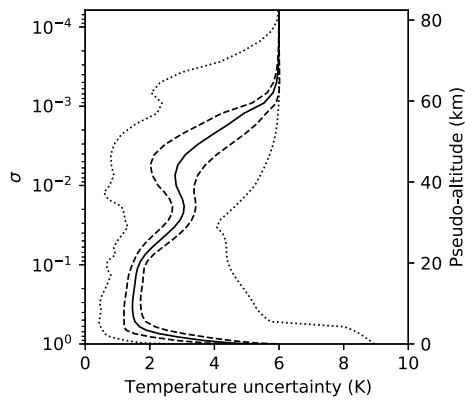


**Figure 1.** Temperature uncertainty in the TIRVIM data set between MY34  $L_s = 182.288^\circ$ – $211.388^\circ$  as a function of  $\sigma = p/p_{\text{surf}}$ . The right y-axis is pseudo-altitude  $z = -H \ln \sigma$ , assuming a scale height of  $H = 8.5$  km, as per the Mars standard atmosphere from the surface to 85 km altitude in Table 4.7 of M. D. Smith et al. (2017) (an underestimate in the lower atmosphere and an overestimate in the middle atmosphere, but it is sufficiently accurate for plotting). We use  $H = 8.5$  km for all pseudo-altitudes in this paper. The solid line is the mean, dashed lines are mean  $\pm 1$  standard deviation, and the dotted lines show the minimum and maximum.

and in Section 3, we describe the model, assimilation scheme, and observation operator. Section 4 describes sensitivity tests done to optimize the assimilation parameters. Section 5 describes the main results of the paper, and in Section 6, we conclude.

## 2. Observations

TIRVIM is a thermal infrared spectrometer designed to observe Mars at wavelengths between 1.7 and 17  $\mu\text{m}$  ( $590$ – $5,900$   $\text{cm}^{-1}$ ) (Korablev et al., 2018). It was designed to be continuously operating during TGO's mission, although in practice this was not possible due to the limited lifetime of the instrument's cryocooler. TIRVIM measured radiance spectra in nadir, from which have been retrieved atmospheric temperature profiles, surface temperatures, dust column optical depths (at  $1,090$   $\text{cm}^{-1}$ ) and water ice column optical depths (at  $820$   $\text{cm}^{-1}$ ). These retrievals are fully described by Guerlet et al. (2022). In this paper we focus on atmospheric temperature and CDOD observations only. TIRVIM operated from MY34  $L_s = 142.79^\circ$  (13 March 2018) until MY35  $L_s = 115.16^\circ$  (2 December 2019), when its cryocooler failed.

TIRVIM took observations at all local times over a 55-sol period. TGO's inclination is  $74^\circ$ , so there are no nadir observations poleward of this latitude in either hemisphere. The temperature profiles have a maximum sensitivity between 5 and 50 km above the ground, and a vertical resolution of about

10 km (Guerlet et al., 2022). The instrument was only sensitive to the true atmospheric temperatures at altitudes of 3–55 km, based on retrieval averaging kernel statistics (see Section 3.3). From the trace of the averaging kernel matrix, the number of degrees of freedom in each temperature retrieval is  $3.3 \pm 0.2$ . The measurement uncertainty, shown in Figure 1, is a function of altitude. It is typically 2–4 K over most of the altitude range, increasing at the top and the bottom of the profile. CDODs typically have an uncertainty of 0.06–0.20 (the 25%–75% range over the assimilated observations, with mean 0.16).

In this paper, we assimilate observations from just before the onset of the MY34 GDS to just after its peak, from  $L_s = 182.288$ – $211.388^\circ$ . Figure 2 shows the data availability and distribution in latitude and local time for this period. These specific start and end points were chosen because there are long gaps in the data immediately before and afterward. There are 312,741 temperature profiles and 214,806 column dust retrievals during this period. There is a gap in the data between  $L_s = 191.567^\circ$ – $194.420^\circ$ , with significantly higher observation density afterward. The local time of day for the majority of observations moves backwards over time; almost all 24 hr of local time are sampled during this period. Exceptions are the northern hemisphere around 4 a.m., and the southern hemisphere around 4 p.m. A significant fraction of TIRVIM observations have missing values for CDOD, as it cannot be retrieved in conditions when the temperature contrast between surface and lower atmosphere is low, which typically occurs near dawn and dusk in non-stormy conditions (see Guerlet et al., 2022). Most of the missing dust retrievals are poleward of  $60^\circ$ , where almost all dust retrievals are removed.

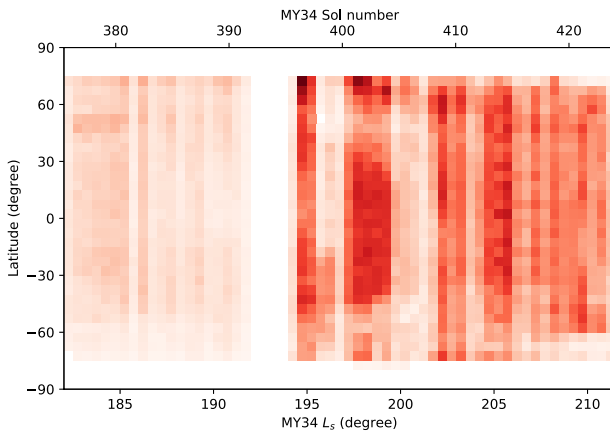
## 3. Methods

### 3.1. Model

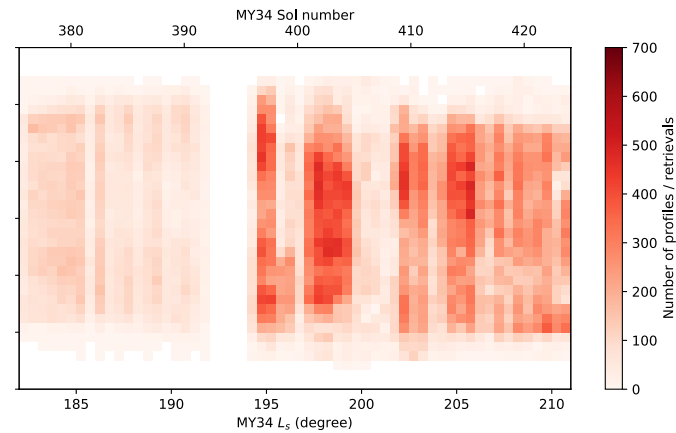
The Mars PCM solves the hydrostatic primitive equations on a rotating sphere alongside parametrizations of many physical processes relevant to Mars (Forget et al., 1999). Most pertinent to the current work is the treatment of dust, which is transported by the model in a two-moment scheme which separately transports a mass mixing ratio (MMR) and the number of dust particles within each grid cell (Madeleine et al., 2011). By transporting these two quantities separately the dust particle size distribution is determined by assuming a log-normal particle size distribution with fixed variance. The Mars PCM has been validated against many observational data sets since the Viking landers in the 1970s (Forget et al., 1999).

We run the model at the standard climate model grid spacing of  $64 \times 48$  points in longitude and latitude, corresponding to  $5.625^\circ \times 3.75^\circ$  horizontal grid spacing. The vertical grid is stretched so there are more points near

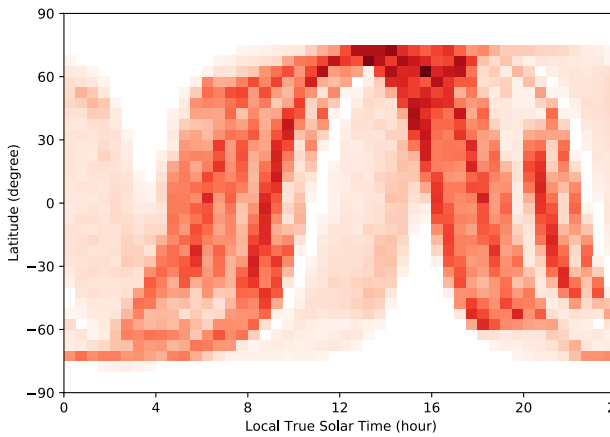
(a) Number of temperature profiles vs  $L_s$  and latitude.



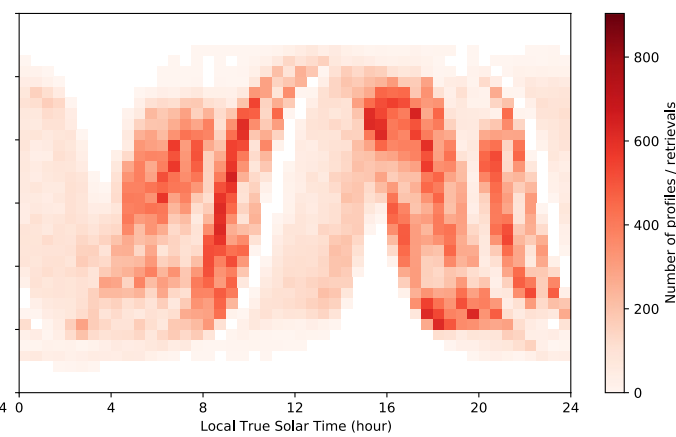
(b) Number of CDOD retrievals vs  $L_s$  and latitude.



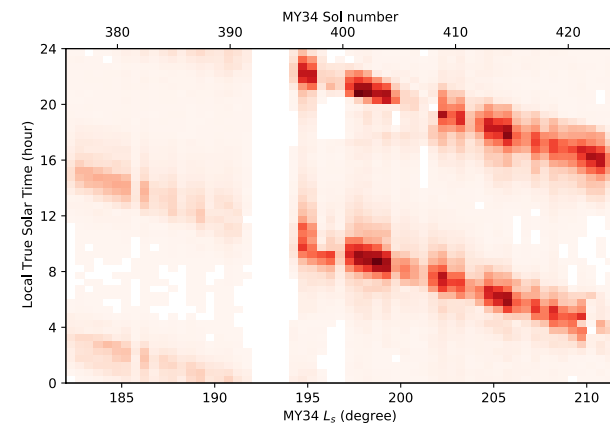
(c) Number of temperature profiles vs local true solar time and latitude.



(d) Number of CDOD retrievals vs local true solar time and latitude.



(e) Number of temperature profiles vs  $L_s$  and local true solar time.



(f) Number of CDOD retrievals vs  $L_s$  and local true solar time.

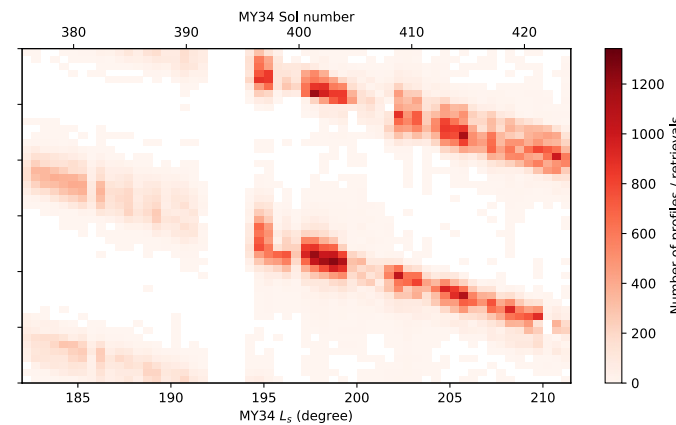


**Figure 2.** Number of TIRVIM temperature profiles (left column (a, c, e)) and column dust optical depth (CDOD) retrievals (right column (b, d, f)) as a function of MY34  $L_s$ , latitude, and local true solar time during the period assimilated in this work. Panels (a and b) versus MY34  $L_s$  and latitude; panels (c and d) versus local true solar time and latitude; and panels (e and f) versus MY34  $L_s$  and local true solar time. Observations are counted in bins with width  $5.0^\circ$  in latitude,  $0.5$  hr in local time, and  $0.5^\circ$  in  $L_s$ ; bins with no observations are white. The upper x-axis shows the equivalent model sol numbers; see Text S1 in Supporting Information S1 for details.

the ground; we use 32 hybrid (sigma-pressure) levels with the lowest level about 4 m above the ground, and the highest level at about 100 km altitude, depending on local conditions (Forget et al., 2017, p. 9). About 12 layers fall within the lowest atmospheric scale height. The model's dynamical time step  $\delta t$  is 1/960 of a sol ( $\sim 94.5$  s), and the physical parametrizations are called every 10 dynamical timesteps (i.e., every physics timestep, 1/96 of a sol, or four times per Martian hour). Text S1 in Supporting Information S1 describes the time axis used in the GCM and how it relates to observation times.

Dust settles throughout the atmosphere, and can fall out of the bottom of the atmosphere onto the surface. When run without assimilation, dust column abundances in the GCM are forced by rescaling at each physics timestep to a global “dust scenario” map based on observed dust opacities, with gaps filled in by kriging (Montabone et al., 2015, 2020). The GCM also injects dust into the lowest atmospheric layer at a constant rate, to (simply) represent dust lifting from the surface, and continuously supply the atmosphere with large-radius particles. Large dust particles fall to the surface faster than small dust particles, and so without a supply of large dust particles, the dust particle size distribution will eventually become unrealistically skewed toward small particles. The injected dust population has effective radius 3  $\mu\text{m}$  and variance 0.5; these parameters and the injection rate were tuned during model development so the particle size distribution in the standalone GCM is stable in time and matches observations.

Water is transported by the model (Pottier et al., 2017), and can condense into water ice clouds, whose particles have an effective radius that varies with local conditions, and which are treated as radiatively active. Dust acts as a source of cloud condensation nuclei, and precipitating water ice can remove dust from the atmosphere by scavenging.

### 3.2. Assimilation Scheme

Assimilation is based on the LETKF, which is a standard method for ensemble data assimilation (Evensen, 2003; Hunt et al., 2007). Full details of the LETKF itself as applied in this context are described in Navarro et al. (2014) and Navarro et al. (2017); here we give a summary and focus on the changes to the scheme since Navarro et al. (2017).

Before starting the assimilation we spin up an ensemble of GCM simulations. This ensemble is used as the forecast for the first assimilation step. Its ensemble mean  $\bar{\mathbf{x}}^b$  is used as the *background* atmospheric state in the assimilation, and the purpose of the ensemble is to estimate the uncertainty in the background state. We use the spread of values to set the background error covariance matrix  $\mathbf{B}$  in the assimilation. For the spin up stage in this case we ran an ensemble of GCM simulations starting at MY34 sol 318 ( $L_s = 150.2^\circ$ ), that is, about 30  $L_s$  before the start of the assimilation period. This gave the ensemble members enough time to spin up to an equilibrium state individually, and to spread out over the model state space such that the standard deviation of the ensemble at each point quantified the uncertainty in the background state. As dust is the major unknown in Mars' atmosphere, and the atmospheric state is so sensitive to it, to generate an ensemble that spans the range of possibilities we ran each spin-up simulation with a different globally fixed visible CDOD. This is enforced during each physics timestep by rescaling the dust MMR in each column. CDOD values for the ensemble members were log-uniformly distributed between 0.05 and 1.5, which spans the typical range of realistic dust column optical depths in non-GDS years (Montabone et al., 2015).

The assimilation step computes an *analysis* ensemble  $\mathbf{x}^{a,i}$ ,  $i = 1 \dots N$ , at the analysis time  $t_a$ , where  $N$  is the ensemble size. Most of the results are presented using the mean of this ensemble, which we shall simply refer to as the *analysis*. The assimilation uses the forecast ensemble as the background state  $\mathbf{x}^{b,i}$ , and observations  $\mathbf{y}_o$  within an assimilation window stretching from  $t_a - t_b$  to  $t_a + t_f$ , where  $t_b$  is the window length backwards in time and  $t_f$  is the window length forward in time. To ensure each observation is used in exactly one assimilation step,  $t_b = t_f = \Delta t/2$ , where  $\Delta t$  is the assimilation cycle length, the time between consecutive assimilation steps. Adaptive covariance inflation is applied to the background ensemble. The observation operator  $H(\dots)$  is applied to the background ensemble, to interpolate the forecasts in space and time to the observation points, and to ensure that the forecast and observations are subsequently compared as if TIRVIM were observing the background state; Section 3.3 provides full details.

To perform the assimilation, at each model grid point we identify observations within  $L_{\text{eh}} = 900$  km horizontally (along a great circle), and within  $L_{\text{ev}} = 0.2\sqrt{6}$  vertically in  $\log(p)$ , a process called localization (Hamill et al., 2001), which significantly speeds up the calculation and also reduces the effects of random noise in the observations acting over large distances. The measurement uncertainty for each observation is modified according to its horizontal ( $d_h$ ) and vertical distance ( $d_v$ ) from the grid point, where  $d_v$  is measured in  $\log p$ . For observation  $l$ , this modified observational uncertainty is

$$\sigma_l^o = \sigma^o \exp\left(\frac{d_h^2}{2L_{\text{ih}}^2}\right) \exp\left(\frac{d_v^2}{2L_{\text{iv}}^2}\right) \quad (1)$$

where  $\sigma^o$  is the unmodified observational uncertainty,  $L_{\text{ih}} = 600$  km is the internal horizontal localization length, and  $L_{\text{iv}} = 0.2$  is the internal vertical localization length.

The LETKF equation for the analysis mean  $\bar{\mathbf{x}}^a$  is (Hunt et al., 2007; Navarro et al., 2017)

$$\bar{\mathbf{x}}^a = \bar{\mathbf{x}}^b + \mathbf{X}^b \tilde{\mathbf{P}}^a (\mathbf{Y}^b)^\top \mathbf{R}^{-1} (\mathbf{y}^o - H(\bar{\mathbf{x}}^b)) \quad (2)$$

where  $\bar{\mathbf{x}}^b$  is the background mean,  $\mathbf{X}^b$  is the matrix whose columns are individual forecast ensemble members minus the ensemble mean, in model space,  $\mathbf{Y}^b$  is the matrix whose columns are individual forecast ensemble members mapped to the observation points minus the ensemble mean, in observation space,  $\mathbf{R}$  is the matrix of observation uncertainties (diagonal) modified by the localization weights above,  $\mathbf{y}^o - H(\bar{\mathbf{x}}^b)$  is the difference between the observations and the forecast mean, in observation space, called the “innovation,” and

$$\tilde{\mathbf{P}}^a = \left[ (N-1)\mathbf{I} + (\mathbf{Y}^b)^\top \mathbf{R}^{-1} \mathbf{Y}^b \right]^{-1} \quad (3)$$

is a normalization factor. The terms before the innovation are essentially the ratio of the background error covariance to the sum of the background and observational error covariances, but for vectors of background forecasts and observations.

Equation 2 can be written as

$$\bar{\mathbf{x}}^a = \bar{\mathbf{x}}^b + \mathbf{X}^b \mathbf{w}^a \quad (4)$$

where  $\mathbf{w}^a$  is a matrix of weights assigned to each ensemble member based on the differences between the forecast and observations, the observational error covariance, and the background error covariance. We are not restricted to using  $\mathbf{w}^a$  to update solely the quantity that is observed;  $\mathbf{w}^a$  can be used to update any prognostic variable. This is only physically sensible where there are correlations between changes in the observed quantity and changes in the other prognostic variable. This can be justified by noting that some quantities are related by known physical laws; for example, the atmospheric temperature and wind structure are related, as are the atmospheric temperature and surface pressure. This assimilation of such *indirectly observed* variables is discussed by Navarro et al. (2017) in detail.

In this work we use atmospheric temperature observations to update the GCM atmospheric temperature field (temperature updates temperature, TuT). We then use  $\mathbf{w}^a$  computed for temperature to update the zonal and meridional velocities (TuW) and the surface pressure (TuPs, using  $\mathbf{w}^a$  at the lowest model grid level).

In most configurations (see below), we also use temperature to update the dust MMR (TuD). Navarro et al. (2014) showed that Mars' observed detached dust layers (Heavens et al., 2011) are reproduced by the assimilation when TuD is employed, as dust modifies the temperature field. TuD is applied only where the correspondence between changes in dust and changes in temperature are strong, that is, where the shortwave heating rate is above  $0.2 \text{ K hr}^{-1}$  and the total insolation is above  $100 \text{ W m}^{-2}$  (this is essentially a constraint on time of day and latitude as a function of time of year). It is also constrained to occur only above pseudo-altitude  $\sim 11$  km, because the correspondence between dust and heating is based on MCS observations, which have systematic biases close to the ground (Navarro et al., 2014). Whenever the dust MMR is updated by the assimilation the dust number is also updated, so that any new dust has a particle size distribution with fixed dust effective radius; this radius is a free parameter of the assimilation scheme.

In the forecast step we step forward the GCM in time, starting from the analysis ensemble, from analysis time  $t_a$  up to  $t_a + \Delta t + t_p$  which is the next analysis time plus the window length forward in time. The cycle then begins anew at the new analysis time  $t_a + \Delta t$ . During the forecast step the GCM runs freely with no constraints on the dust field. In the assimilation experiments the only processes that can add or remove dust from the atmosphere are the assimilation step and sedimentation onto the surface.

### 3.3. Observation Operator Using Averaging Kernels

The comparison between forecast and observations  $\mathbf{y}^o - H(\mathbf{x}^b)$  is a crucial part of the data assimilation process. This comparison must compare like-with-like to minimize representation errors and ensure that forecast errors are calculated accurately. The observation operator must not only interpolate the forecast to the observation locations, but also reproduce what TIRVIM would observe if it were to observe the forecast atmosphere. When retrievals are used, the correct way to do this is to use the same averaging kernels and prior profile that were used in the retrieval (R. N. Hoffman, 2011; Rodgers & Connor, 2003).

We have improved on earlier versions of this assimilation scheme by basing the observation operator for atmospheric temperature on the TIRVIM retrieval averaging kernels. Earlier work using this scheme by Navarro et al. (2017) had no vertical smoothing in the observation operator. This was (reasonably well) justified as they assimilated limb observations from MCS, which have a vertical resolution of about 5 km (Kleinböhl et al., 2009), similar to the model's vertical grid spacing throughout most of the atmosphere. Nadir measurements have a coarser vertical resolution, so some smoothing of the forecast profile is required.

We believe this is the first time averaging kernels have been applied directly in Mars data assimilation. Lee et al. (2011) recommend their use for assimilation of Thermal Emission Spectrometer (TES) retrievals, without actually using them. Lewis et al. (2007) used a more general vertical smoother for assimilation of TES retrievals, as have others using the same assimilation scheme.

Before the averaging kernels are applied, we interpolate from the forecast grid to each observation location linearly in longitude, latitude, and time, and then vertically to the observed  $\sigma$  coordinates, linearly in  $\log \sigma$ .

The averaging kernels quantify the relative contributions to each point in a retrieved profile from the true and prior atmospheric states at each altitude. The vertical width of the averaging kernel sets the true vertical resolution of the instrument. The retrieval  $\mathbf{y}^o$  is related to the true atmospheric state  $\hat{\mathbf{x}}$  and the prior profile  $\mathbf{x}^p$  by the averaging kernels  $\mathbf{A}$  (Rodgers & Connor, 2003) such that

$$\mathbf{y}^o = \mathbf{x}^p + \mathbf{A} (\hat{\mathbf{x}} - \mathbf{x}^p) \quad (5)$$

A perfect retrieval has  $\mathbf{A} = \mathbf{I}$ , in which case  $\mathbf{y}^o = \hat{\mathbf{x}}$ , with no prior information retained. A retrieval that contains no information from the true atmospheric state has  $\mathbf{A} = \mathbf{0}$ , in which case  $\mathbf{y}^o = \mathbf{x}^p$ . Real instruments are somewhere in between, and  $\mathbf{A}$  is a strong function of altitude.

To assimilate a retrieval, the observation operator  $H(\mathbf{x}^b)$  is a slightly modified form of Equation 5:

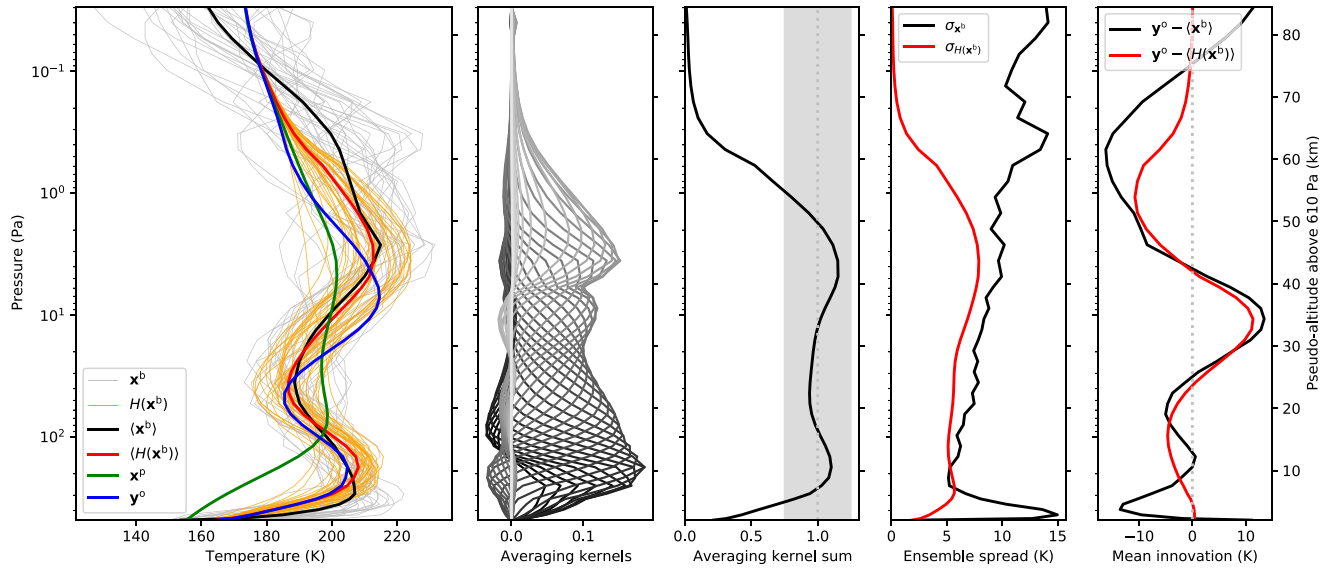
$$H(\mathbf{x}^b) = \mathbf{x}^p + \mathbf{A} (\mathbf{x}^b - \mathbf{x}^p) \quad (6)$$

where  $\mathbf{x}^b$  is the background profile interpolated to the retrieved profile levels. The result is a “retrieved forecast,” that is, what a retrieval of a hypothetical TIRVIM spectrum would look like if it observed the forecast atmosphere.

Figure 3 shows two examples of this observation operator applied to a real forecast of TIRVIM retrievals. Figure 3a is a “good” case near the top of the range of retrieval degrees of freedom (3.97), and Figure 3b is a “bad” case at the low end of the range (2.62). As TIRVIM is a nadir sounder, the averaging kernels (second column) are quite broad, and the “retrieved forecast” ensemble and ensemble mean are smoother than the raw forecast ensemble and ensemble mean.

The retrieved temperature profile and the retrieval prior converge at the top of the profiles, indicating that almost all the information in the retrieval comes from the prior there, and so we should avoid assimilating this part of the profile. After the observation operator is applied to the forecast ensemble (Equation 6), at the top of profile the ensemble collapses onto the retrieval prior, so differences between the forecast and retrieved temperature profiles are artificially small in this region (note also the change in ensemble spread in the fourth column of Figure 3

(a)  $L_s = 208.86^\circ$ , longitude  $34.53^\circ\text{E}$ , latitude  $64.94^\circ\text{S}$ , LTST 2.24.



(b)  $L_s = 208.84^\circ$ , longitude  $108.94^\circ\text{W}$ , latitude  $40.82^\circ\text{N}$ , LTST 15.87.

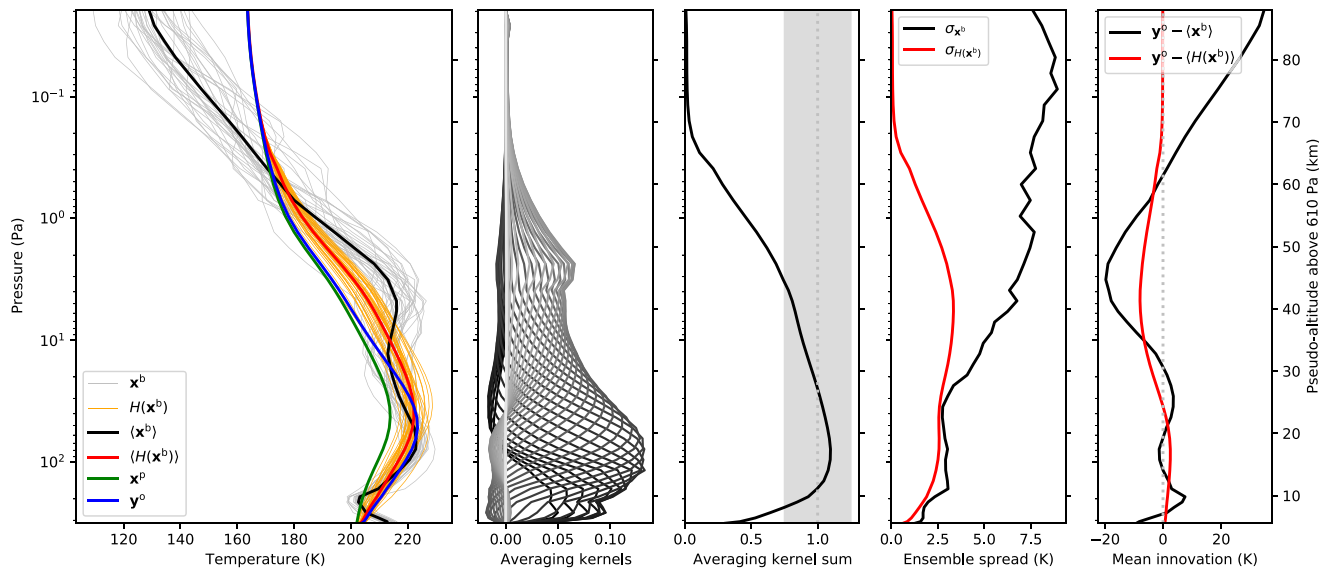


**Figure 3.** Demonstration of the observation operator acting on the ensemble forecast for two temperature profiles retrieved from TIRVIM radiance spectra. (a)  $L_s = 208.86^\circ$ , longitude  $34.53^\circ\text{E}$ , latitude  $64.94^\circ\text{S}$ , local true solar time 2.24, retrieval degrees of freedom 3.97; (b)  $L_s = 208.84^\circ$ , longitude  $108.94^\circ\text{W}$ , latitude  $40.82^\circ\text{N}$ , local true solar time 15.87, retrieval degrees of freedom 2.62. The left panel shows the raw forecast ensemble members and ensemble mean (thin gray lines and thick black line, respectively), forecast ensemble members and ensemble mean after the observation operator is applied (thin orange lines and thick red line, respectively), retrieval prior (thick green line), and the retrieved temperature profile, that is, the “observations” (thick blue line). From left to right, the other panels show: (1) full set of averaging kernel functions, indicated by different greyscale shades; (2) sum over the averaging kernels, where the shaded region indicates the range 0.75–1.25, and the dotted line indicates 1; (3) ensemble spread for the raw forecast ensemble (black) and the forecast ensemble after the observation operator is applied (red); and (4) the mean innovation, that is, the retrieved temperature profile minus the ensemble mean, showing this for the raw ensemble mean (black) and the ensemble mean after the observation operator is applied (red).

before and after Equation 6 is applied). Conversely, lower in the profiles, most or all of the spread in the forecast ensemble is preserved by the observation operator, hence in this region the difference between the forecast temperature profile and the retrieved temperature profile is real, and so we should include such observations in the assimilation.



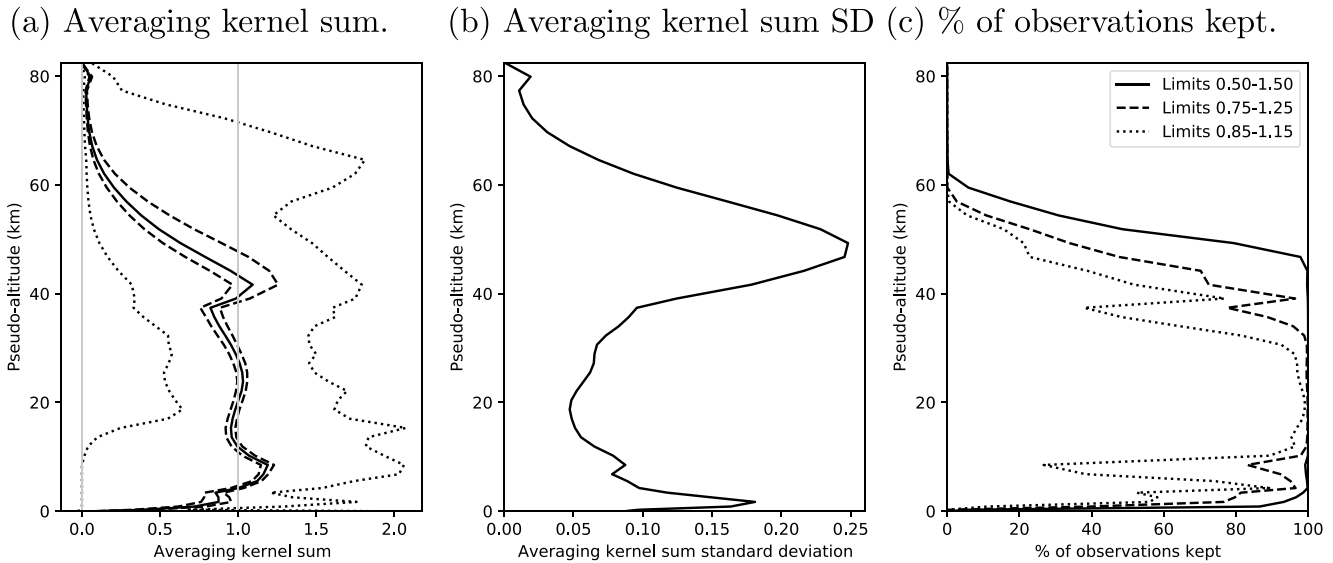


**Figure 4.** Averaging kernel sum statistics for TIRVIM temperature retrievals between MY34  $L_s = 182.288^\circ$ – $211.388^\circ$ , as a function of pseudo-altitude. (a) Sum over averaging kernels. The black dotted lines are the minimum and maximum, the solid line is the median, the dashed lines are the 25th and 75th percentiles, and the vertical gray lines indicate 0 (all weight on the prior) and 1 (all weight on the measured radiances). (b) Standard deviation of averaging kernel sums. (c) Percentage of observations kept when an averaging kernel sum filter is applied.

To distinguish between these two cases, and quantify how much information comes from the prior and the true atmospheric state, we use the sum over the averaging kernels at each level (Figure 3, third column). It is a general property of averaging kernels that, where the averaging kernel sum is near zero, all the information in the retrieval comes from the prior, and where the averaging kernel sum is close to one (e.g., at 10 Pa), almost all the information in the retrieval comes from the observed radiances. Therefore a suitable way to distinguish between these two cases is to impose a filter on the averaging kernel sum at each level of the temperature profile, and only assimilate observations whose averaging kernel sum falls within a particular range. This ensures that observations which are assimilated contain as much information from the observed radiances as possible, and as little information from the retrieval prior. The gray band in the third column of Figure 3 identifies the levels that would be retained if a filter of 0.75–1.25 were applied. The main practical difference between the two cases in Figures 3a and 3b is that the vertical range of retained observations extends higher in the atmosphere when the retrieval degrees of freedom are higher.

Figure 4 shows averaging kernel sum statistics for TIRVIM temperature retrievals between MY34 sols 376–424. Between 5 and 40 km a large majority of the profiles have averaging kernel sums close to one, and even between 1 and 50 km in many cases. Figure 4c shows how much of the data set remains when various filters are applied. Between 10 and 30 km almost all observations are kept, whatever the condition. The largest differences are between 40 and 60 km, where imposing strict limits of 0.85–1.15 removes at least 50% of the observations, and also in a narrow band of altitudes around 5–10 km. If the filter is relaxed slightly to 0.75–1.25, then most of the observations that were rejected for the strict limits are included.

### 3.4. Column Dust Optical Depth Assimilation

The second major update to our scheme is to assimilate CDODs (denoted CuD, i.e., column-updates-dust). CDODs have been assimilated by others previously (Lewis & Barker, 2005; Montabone et al., 2014; Ruan et al., 2021), but were not used by Navarro et al. (2014, 2017) in previous work with this scheme. They used MCS observations, and MCS is a limb scanner that does not measure CDOD directly as it rarely sounds the dust profile all the way to the ground. TIRVIM dust retrievals do have to make some assumptions about the vertical dust distribution, which is a limitation of TIRVIM data, but as a nadir instrument it does view the full atmospheric column.

Guerlet et al. (2022) assume dust is well-mixed in the lowest two scale heights and that its mixing ratio decreases linearly with  $\log(p)$  above. A quality flag is assigned to each CDOD observation, related to the sensitivity of

the radiance to changes in dust load. Above warm surfaces, dust retrievals are quite reliable, but above colder surfaces, there can be systematic biases and non-unique solutions depending on the assumed dust vertical distribution. Only retrievals with a good quality flag are assimilated; this excludes about a third of the CDOD retrievals (Figure 2).

We forecast the CDOD at the TIRVIM frequency of  $1,090\text{ cm}^{-1}$  using the forecast dust MMR profile. For each available column dust observation we interpolate the forecast dust MMR field to the observation longitude, latitude, and time. We then integrate the total dust column opacity in the vertical based on Equation 1 of Madeleine et al. (2011):

$$\tau_{\text{dust}} = \sum_{k=1}^K \frac{3}{4} \frac{Q_{\text{ref}} q_k}{\rho_p r_{\text{eff}} g} \Delta p_k \quad (7)$$

where  $\tau_{\text{dust}}$  is the CDOD;  $K$  is the total number of model levels;  $Q_{\text{ref}} = 1.53112$  is the effective dust extinction coefficient at the TIRVIM wavelength, that accounts for integration over a dust particle size distribution with dust effective radius  $r_{\text{eff}} = 1.5\text{ }\mu\text{m}$  and effective variance  $\nu_{\text{eff}} = 0.3$ ;  $q_k$  is the dust MMR at level  $k$ ;  $\rho_p = 2,500\text{ kg m}^{-3}$  is the dust density; and  $\Delta p_k$  is the pressure thickness of model level  $k$ . We made some of the same assumptions as in the retrieval, such as using the same fixed  $Q_{\text{ref}}$  and  $r_{\text{eff}}$ , but in the GCM  $r_{\text{eff}}$  is a function of location, and the GCM does not assume any particular vertical dust distribution, so these restrictions could be relaxed in future.

Once CDOD is forecast at each observation location, observations are assimilated into the GCM CDOD field using the LETKF in the same way as for atmospheric temperature (Equation 2), except vertical weighting is not required. As CDOD is not a prognostic variable in the Mars PCM, once we have the CDOD analysis we adjust the dust MMR profile so that its CDOD is the same as the CDOD analysis. As CDOD varies linearly with dust MMR this is a simple linear rescaling of the atmospheric dust profile. This is reasonable as even during a GDS  $r_{\text{eff}}$  and hence  $Q_{\text{ref}}/r_{\text{eff}}$  do not change substantially compared with changes in  $q$  (Madeleine et al., 2011, Figure 2). The dust number is also updated, as described at the end of Section 3.2.

We ran two versions of the dust assimilation. In the first case (CuD), we just used the CDOD observation to update the dust column abundance. In this case, we might expect the vertical dust distribution not to reflect the real vertical dust distribution, as the model does not generate detached dust layers spontaneously. We try to avoid this problem with our second version (TuD-CuD), which combines the direct assimilation of CDOD with an indirect update of the dust profile using temperature (TuD). First, we perform the TuD step, and then assimilate CDOD. The TuD step should produce a more accurate vertical dust distribution than the model alone, and the column dust assimilation constrains the total amount of dust in each column using real observations. The order of operations is important here: TuD must be done first and CuD second, because otherwise the total amount of dust in the column will not be the amount that is assimilated from observations; if we assimilate CDOD first there is no guarantee that the TuD step will conserve the total amount of dust in the column. This is similar to Ruan et al. (2021), who assimilated MCS dust profiles alongside TES and THEMIS dust column abundances, but note we do not assimilate the dust vertical distribution directly, but only infer it from changes in temperature.

#### 4. Sensitivity Analysis

The assimilation scheme has several tuneable parameters. To optimize the temperature assimilation we performed sensitivity tests running short assimilations during the onset of the MY34 GDS (i.e., the period during which the dust concentrations are changing most rapidly). We varied four parameters, and ran an assimilation for each combination of values, 72 in total. We varied the number of ensemble members  $N$  (18, 36, and 72), the length of the assimilation cycle  $\Delta t$  (2, 3, 6, and 12 hr), the threshold on the averaging kernel sum filter (0.50–1.50, 0.75–1.25, and 0.85–1.15), and the effective radius of new dust added to the model  $r_{\text{eff}}$  (1.0 and 1.5  $\mu\text{m}$ ).

The goal of the ensemble is to sample the range of uncertainties in the forecast model. However, the ensemble is finite, and the mean and covariance of a finite ensemble will differ from the mean and covariance of an infinitely large ensemble. If an infinitely large ensemble spanning all possible atmospheric states has mean  $\bar{x}$  and variance  $\sigma^2$ , then an ensemble of size  $N$  will have an expected error in the ensemble mean of  $\sigma/\sqrt{N}$ , and an expected error in the ensemble variance of  $\sigma^2\sqrt{2/(N-1)}$  (Ahn & Fessler, 2003). Hence if the ensemble is too small then

outlying values and noise will have a disproportionately large influence on the ensemble mean and variance, so we expect the assimilation to be more accurate for larger ensembles. This is an important part of the rationale for using localization in LETKF assimilation (Hamill et al., 2001). Conversely, larger ensembles consume more resources, and we might expect the forecast step to be more unstable, as the simulations span a larger (and hence more extreme) range of atmospheric states.

There is a trade-off when choosing the assimilation cycle length between the forecast length and the number of grid points that are updated during each cycle. When the cycle is short, the model has less time to diverge from reality. For Mars the forecast error can saturate in 3–6 hr (Navarro et al., 2017, Figure 2). But when the analysis cycle is longer a larger fraction of the model grid points are updated during each analysis. This is particularly important for assimilation of tracer quantities such as dust, because the only way that new dust is added to the model state is during the assimilation step.

Figure 4c shows different averaging kernel sum filter limits. The very narrow range (0.85–1.15) excludes many observations near 10 and 40 km pseudo-altitude, the moderate range (0.75–1.25) encompasses those observations, and the wide range (0.5–1.5) includes a lot of observations, but some will have 50% of their information content from the prior profile.

The dust effective radius  $r_{\text{eff}}$  for new dust added to the analysis state is tested for 1.0  $\mu\text{m}$ , because Navarro et al. (2017) use this value, and 1.5  $\mu\text{m}$ , because the dust retrievals we assimilate use that value (Guerlet et al., 2022). Dust with smaller radius takes longer to sediment and fall out onto the surface.

We ran each test assimilation from sols 397–407 ( $L_s = 194.8^\circ\text{--}200.9^\circ$ ), using the TuTD configuration (i.e., no CDOD assimilation), and we compared the results with TIRVIM and MCS temperature profiles. We interpolated the analysis in time and space to the TIRVIM (on  $\sigma$  levels) and MCS (on pressure levels) observations. To compare with TIRVIM we applied the averaging kernel operator and the averaging kernel sum filter. We did not apply any vertical smoothing before making the comparison with MCS observations, as the vertical resolution of those observations is comparable with the grid level spacing. We then computed the bias and the root-mean squared error (RMSE) over various pseudo-altitude ranges for TIRVIM (0–10, 10–30, and 30–50 km) and various pressure ranges for MCS (100–1,000, 10–100, 1–10, 0.1–1, and 0.01–0.1 Pa). Time series for each of the 72 test assimilations are shown in Figure 5. Because we ran every possible combination of parameters, we were also able to plot individual comparisons between cases varying just one parameter with all others held constant. These are shown in Figure 6. In both figures we only show select cases where there were significant differences (gauged by eye) between parameter values.

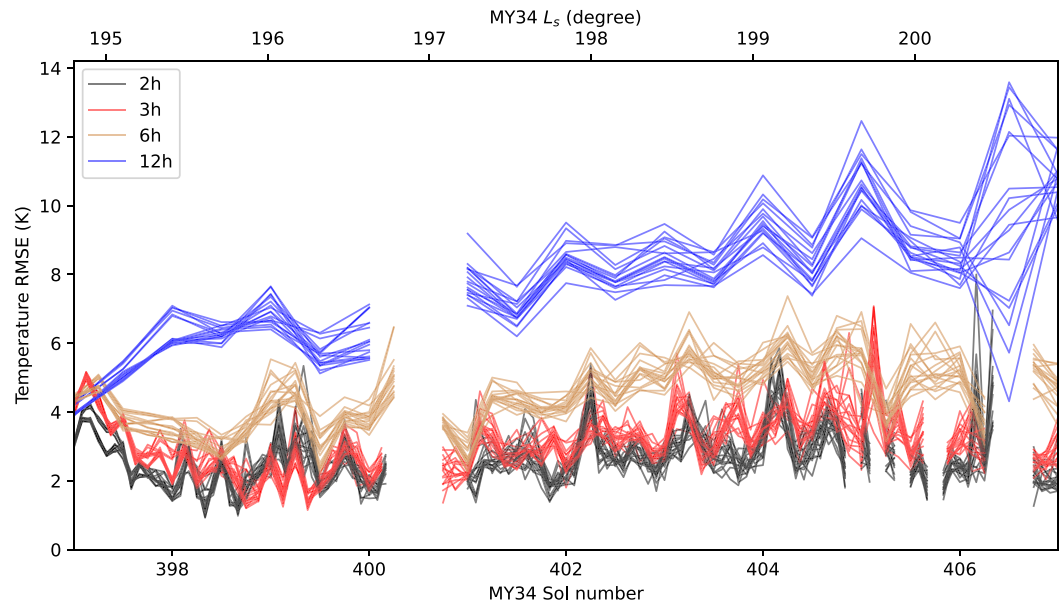
The clearest difference is between the assimilation cycle lengths. Over altitude ranges where TIRVIM is sensitive (i.e., up to 50 km), the shorter the cycle the better the match to observations. Figure 5a shows a representative set of RMSE time series, and Figure 6b shows scatter plots, both verifying against TIRVIM. This trend remains when compared against MCS, although it is not as strong. A clearer trend when verifying against MCS is that  $r_{\text{eff}} = 1.0 \mu\text{m}$  for new dust is generally better than 1.5  $\mu\text{m}$ , particularly for 1–100 Pa (i.e., where the TIRVIM observations are), as illustrated in Figures 5b and 6d. This is consistent with the 1.06  $\mu\text{m}$  radius used in the MCS retrievals (Heavens et al., 2011).

The ensemble size makes a smaller difference, but overall both  $N = 36$  and 72 produce lower RMSE than  $N = 18$  (Figure 6a). The differences between the averaging kernel sum filters are smaller still (Figure 6c); 0.50–1.50 clearly performs the worst, but there is no visible difference between 0.75–1.25 and 0.85–1.15.

The only parameter that had any effect on the practical aspects of running the assimilation was the ensemble size. The clock time to assimilate 1 sol of data was strongly correlated with ensemble size, with  $N = 72$  taking 38–58 min (5–95th percentiles over all  $N = 72$  cases) while  $N = 36$  took 25–39 min and  $N = 18$  took 22–34 min. The forecast step run time depends on the maximum time for any one ensemble member to finish, so the more ensemble members there are, the longer this is. The number of times individual forecast members became unstable was significant only for  $N = 72$  (1.2–13.6 times per sol, compared with 0.1–1.2 for  $N = 36$ ). We had planned to run a series of tests with  $N = 108$ , but chose not to do so as a result.

In conclusion,  $r_{\text{eff}} = 1.0 \mu\text{m}$  for new dust was generally better than 1.5  $\mu\text{m}$ . An averaging kernel sum filter of 0.75–1.25 was better than 0.5–1.5 in most cases, and marginally better than 0.85–1.15 in some cases. As it allows more observations to be assimilated over a wider range of altitudes, we chose the more inclusive 0.75–1.25 condi-

(a) Verification against TIRVIM at 10–30 km pseudo- $z$ , coloured by cycle length.



(b) Verification against MCS at 10–100 Pa, coloured by new dust effective radius.

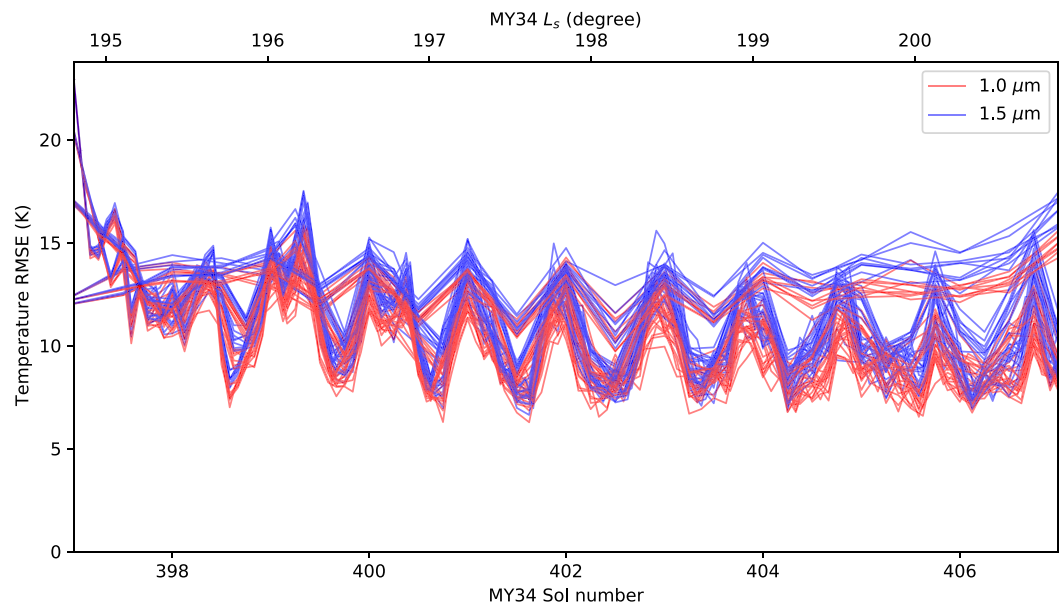


**Figure 5.** Time series showing root-mean squared error for short test assimilations verified against (a) TIRVIM temperature observations at 10–30 km pseudo-altitude, and (b) Mars Climate Sounder (MCS) temperature observations at 10–100 Pa. In panel (a), the lines are color-coded by the length of the assimilation cycle, and in panel (b) they are color-coded by the dust effective radius used for new dust. The different lines for a given color correspond to variations in the other three parameters.

tion. An ensemble size of  $N = 36$  was better than  $N = 18$  in most cases.  $N = 36$  and  $N = 72$  were very similar, but  $N = 72$  required lots of manual restarts and had more model instability in the forecast step, so we chose  $N = 36$  ensemble members. Finally, a 2-hr cycle length was better than 6- and 12-hr in most cases. It was also better than 3 hr in some cases, when compared with TIRVIM observations, but 2- and 3-hr cycles were generally similar. As a 2-hr cycle provides higher time resolution in the final data product, we chose  $\Delta t = 2$  hr.

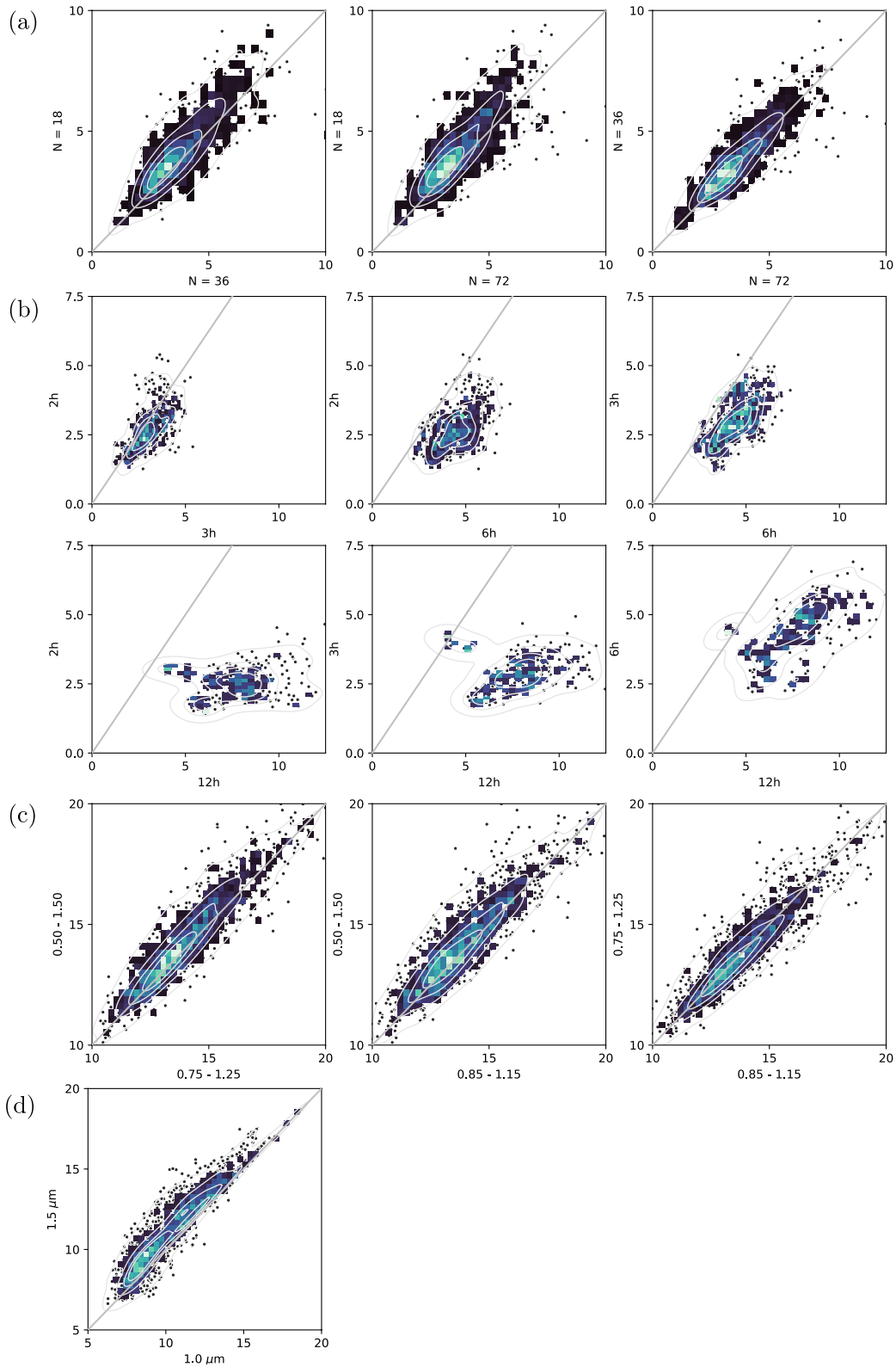


Figure 6.

## 5. Results

We ran three versions of the assimilation between sols 376–424 of MY34, encompassing the onset and peak of the GDS. These were TuTD (temperature updates temperature and dust profile), TuT-CuD (temperature updates temperature, and then column dust updates the dust column and hence the dust profile), and TuTD-CuD (temperature updates temperature and dust profile, and then column dust updates the dust column and hence the dust profile). The assimilation period splits nicely into three distinct segments: before the storm (sols 376–385,  $L_s = 182.3^\circ$ – $187.6^\circ$ ); during the onset of the storm (sols 385–410,  $L_s = 187.6^\circ$ – $202.7^\circ$ ); and at the peak of the storm (sols 410–424,  $L_s = 202.7^\circ$ – $211.4^\circ$ ).

In assimilation experiments it is usual to compare the analysis with a free running model as a control. Alongside the three assimilations we ran a “GCM ensemble” of Mars PCM simulations without assimilation, where the dust column abundances are constrained to match the MY34 dust scenario (Montabone et al., 2015, 2020). This is not a true free-running model, but it is the standard configuration for the Mars PCM and for Mars GCMs in general at present. If the Mars PCM is run without such constraints then dust will sediment out and the model will crash after O(10 sols) as the lack of airborne dust leads to extremely low atmospheric temperatures. When the GCM is run with a dust scenario, dust is added and removed from the atmosphere by rescaling to the column abundances, by dust injection into the lowest layers of the model (which occurs at a constant rate), and by sedimentation onto the surface. The results below use the mean of this ensemble when referring to the “GCM ensemble.”

One additional complication is that the dust scenario used in the GCM ensemble is based on MCS observations. So when our analyses are verified against MCS observations and the assimilation’s performance compared against the GCM ensemble, the comparison between the GCM ensemble and MCS observations is more like an “in-sample comparison,” while the comparison between the analyses and MCS observations is a completely independent verification. When we assimilate CDODs directly, the comparison between our analyses and the GCM ensemble is a fairer comparison than when they are not assimilated.

### 5.1. In-Sample Verification Against TIRVIM Observations

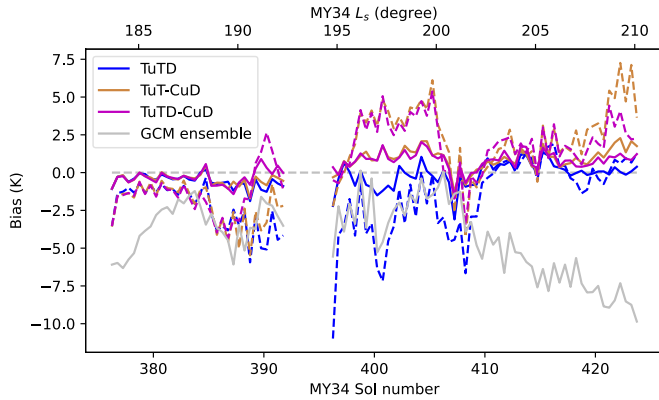
We computed the forecast and analysis bias and RMSE with respect to the TIRVIM observations that were assimilated, as described in Section 4, and over the same vertical ranges. We also computed CDOD at  $1,090 \text{ cm}^{-1}$  from the forecasts and analysis using Equation 7, and verified them against TIRVIM CDOD observations (i.e., with fixed  $Q_{\text{ref}}$  and  $r_{\text{eff}}$ ).

Figure 7 shows the temperature bias and RMSE, and Figure 8 shows the CDOD bias and RMSE. In both fields the analysis RMSE is typically 50% of the forecast RMSE, and the analysis bias is close to zero, showing that the assimilation reduces the error by adding observational information to the system. The temperature RMSE is close to the observed uncertainty (Figure 1). There is no systematic bias in the analyses at any altitude. The forecasts typically have a cool bias below 10 km altitude, and between 30 and 50 km in the TuTD case there is a cool bias while in the other two cases there is a warm bias from about sol 398 onwards. The GCM ensemble is generally biased cool before the dust storm begins, and once the dust storm begins it is biased warm at 0–10 km and cold at 30–50 km. There is a gap in the data between sols 391.7126–396.4636, after which the forecast RMSE is temporarily high, but returns to an equilibrium after about 1 sol (note this also quantifies the convergence time for the assimilation).

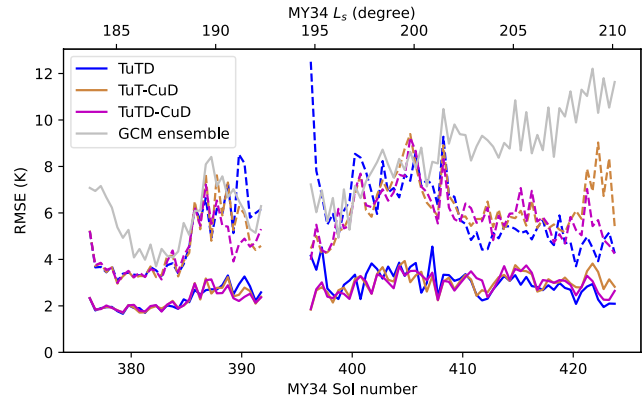
For the CDOD observations, when dust is assimilated the error reduction by the assimilation is about 50% before the GDS begins, and 20%–40% once the GDS has begun. In the TuTD case (where no dust observations are assimilated, so this is an out-of-sample verification), the error reduction is close to zero, except at the peak of the storm. There is a significant negative bias in the TuTD case (i.e., significantly less dust in the analysis than in the TIRVIM observations). When dust is assimilated directly the analysis error is significantly less, leaving a small negative bias of about 0.1–0.2 in each case. This is comparable with the typical uncertainty in the CDOD

**Figure 6.** Scatter plots showing temperature root-mean squared error comparisons between 10-sol test assimilations, varying one parameter at a time. Each dot corresponds to a single analysis. Filled and line contours indicate point density, and individual points are outliers. Equality is the diagonal gray line, and all axes are in K (note not all go to zero). In panel (a) ensemble size  $N$  is varied, verifying against TIRVIM at 30–50 km; (b) varies the assimilation cycle length  $\Delta t$ , verifying against TIRVIM at 10–30 km; (c) varies the averaging kernel sum filter range, verifying against Mars Climate Sounder (MCS) at 10–100 Pa; and (d) varies the effective radius for new dust  $r_{\text{eff}}$ , verifying against MCS at 1–10 Pa.

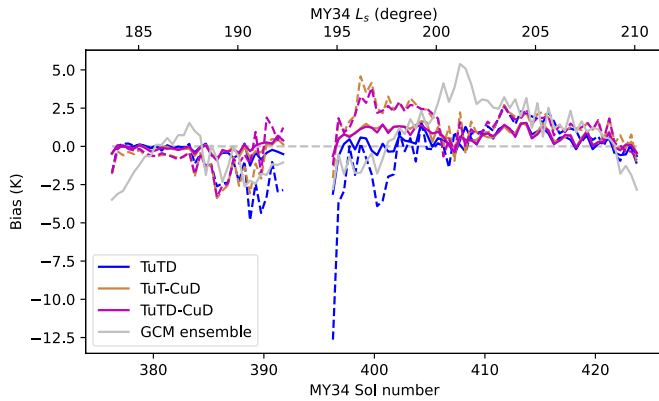
(a) Bias, 30–50 km.



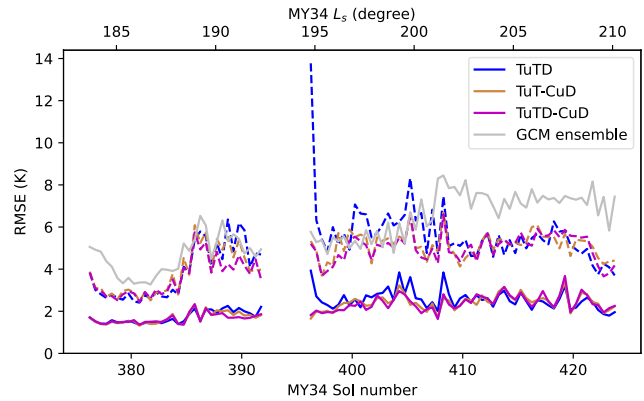
(b) RMS error, 30–50 km.



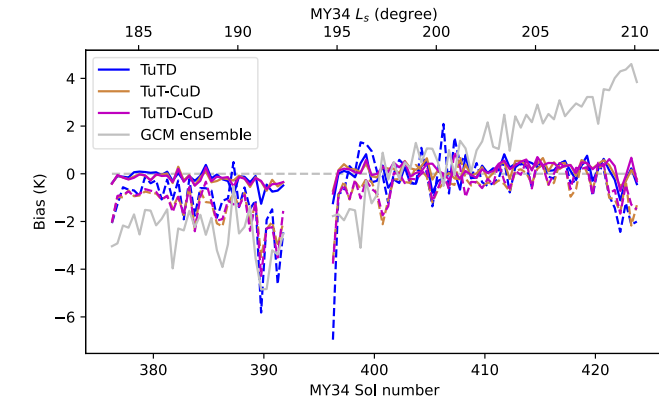
(c) Bias, 10–30 km.



(d) RMS error, 10–30 km.



(e) Bias, 0–10 km.



(f) RMS error, 0–10 km.

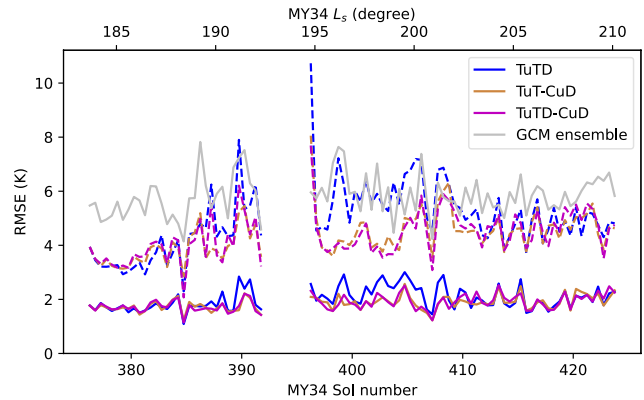


**Figure 7.** In-sample verification against TIRVIM temperature profiles. The left column (a, c, e) shows the bias (analysis/forecast—observations) and the right column (b, d, f) shows the root-mean squared (RMS) error. Data are split by pseudo-altitude: (a and b) 30–50 km; (c and d) 10–30 km; and (e and f) 0–10 km. Solid lines show the analysis mean, and dashed lines show the forecast mean. TuTD is blue, TuT-CuD is brown, TuTD-CuD is magenta, and the GCM ensemble is gray. Data are averaged over 0.5-sol bins.

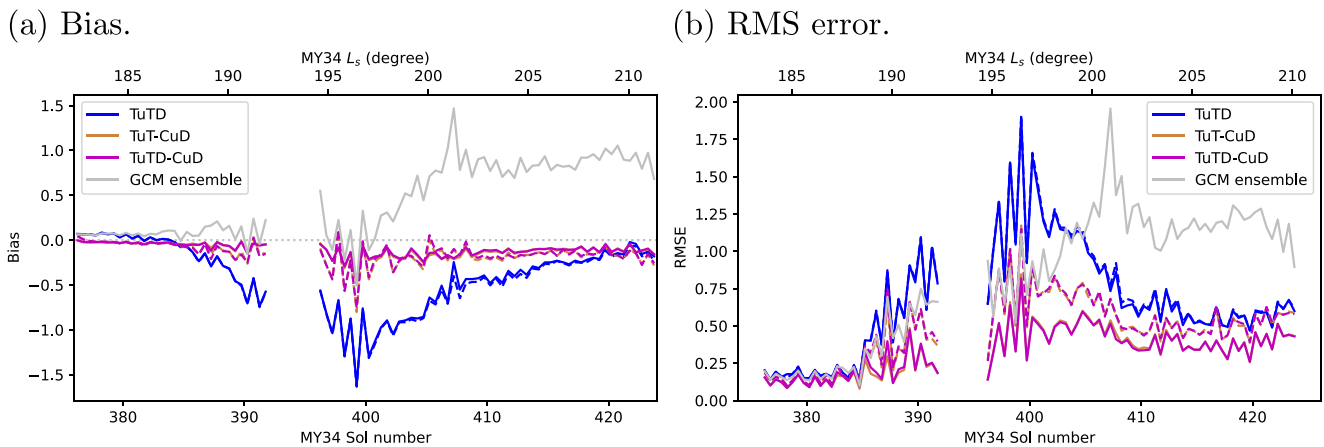


**Figure 8.** Same as Figure 7, but showing in-sample verification against TIRVIM extinction column dust optical depths. Solid lines show the analysis mean, and dashed lines show the forecast mean.

measurements (mean 0.16 over this study period) The GCM ensemble has a strong positive bias (about 1.0) compared with the TIRVIM CDOD observations at the peak of the storm.

## 5.2. Out-of-Sample Verification Against MCS Observations

We verified the analysis and forecast means against MCS temperature observations as described in Section 4. We also computed the dust density-scaled opacity (DSO) in extinction at 21.6  $\mu\text{m}$  (Equation 7 from Madeleine et al. (2011)):

$$\tau_{\text{DSO}} = \frac{3}{4} \frac{Q_{\text{ref}}(r_{\text{eff}})q}{\rho_{\text{dust}}r_{\text{eff}}} \quad (8)$$

where in this case both  $r_{\text{eff}}$  and  $Q_{\text{ref}}$  take the local dust effective radius into account.

Figures 9 and 10 show bias and RMSE time series for temperature and dust DSO, over pressure ranges where the assimilated TIRVIM observations typically lie. These results are clearly poorer than the in-sample verification against TIRVIM observations, but that is not surprising. However, it is important to identify and understand the degree to which they are poorer.

The GCM ensemble, which is constrained by CDOD derived from MCS dust opacities, has a bias and RMSE that falls within the range of values from the three cases assimilating TIRVIM observations. This is encouraging because it implies that, while the absolute errors are larger than when compared with TIRVIM observations, the out-of-sample comparison is comparable with what is effectively an in-sample comparison between the GCM ensemble and MCS observations.

Before the storm there is little difference between the bias and RMSE in the three cases where TIRVIM observations are assimilated. Lower in the atmosphere than 100 Pa, the temperature analysis (as well as the GCM ensemble) has a cold bias of 2–8 K in all cases; we note that when dust observations are assimilated this bias is closer to zero. Higher in the atmosphere than 100 Pa, the TuTD case has a cold bias during the onset of the storm, while the TuT-CuD and TuTD-CuD cases have a warm bias during that period, with the three cases converging at the peak of the storm. Similarly, during the onset of the storm the RMSE in the TuTD case is significantly poorer than in the two other assimilation cases, showing that it is crucial to assimilate some information about dust when it is changing quickly.

There is significantly lower dust DSO during the onset of the storm in the TuTD case than in the MCS observations, at all pressure ranges shown (Figure 10). For TuT-CuD and TuTD-CuD there is, on average, a higher dust DSO than in the MCS observations during the onset of the storm, and by the peak of the storm the bias is close to zero between 10 and 100 Pa and positive in the other two ranges. The GCM ensemble overestimates the amount of dust below the 100 Pa pressure level, and underestimates it above. At all altitudes the RMSE increases from



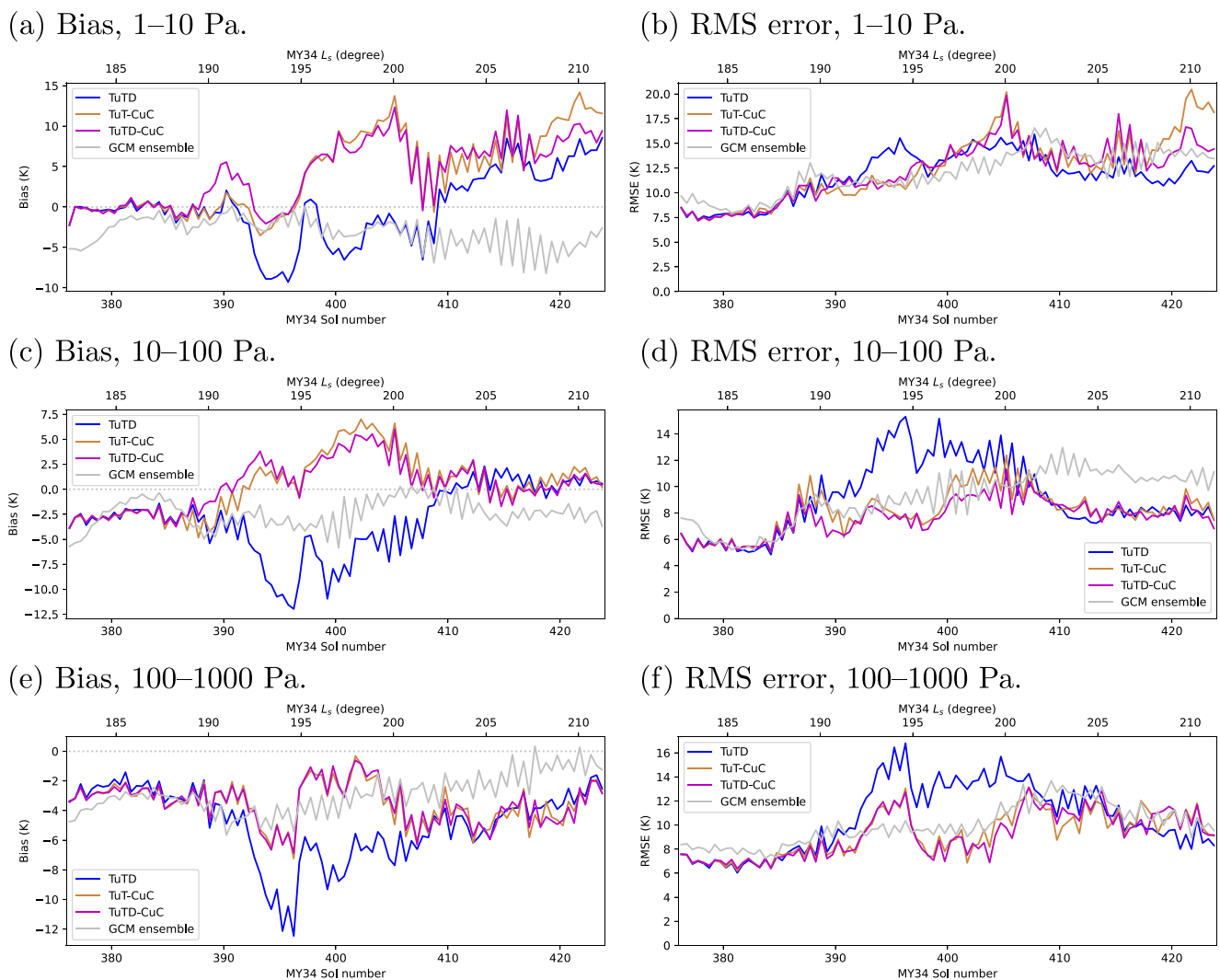


**Figure 9.** Independent verification against Mars Climate Sounder temperature profiles. The left column (a, c, e) shows the bias (analysis/forecast—observations) and the right column shows the root-mean squared error (RMSE) (b, d, f). Data are split by pressure ranges: (a and b) 1–10 Pa; (c and d) 10–100 Pa; and (e and f) 100–1,000 Pa. Each line shows the analysis mean, or the mean of the Global Climate Model ensemble. TuTD is blue, TuT-CuC is brown, TuTD-CuC is magenta, and the GCM ensemble is gray. Data are averaged over 0.5-sol bins.

a low level before the onset of the storm, and increases thereafter. As for temperature, we note that the RMSE in the three analyses is comparable with the RMSE in the GCM ensemble.

The amount of dust in the atmosphere is considerably more when dust observations are assimilated, and so the heating effect of more dust helps to explain why, on average, the cases assimilating dust are warmer than the TuTD case. At the peak of the dust storm the analysis temperature bias in all three cases between 10 and 100 Pa is close to zero, while the GCM ensemble has a cold bias. This is possibly because the GCM ensemble does not exhibit detached dust layers, with its dust distribution monotonically decreasing upwards, so the dust is more concentrated at the surface, heating the lowest atmospheric layers and cooling the higher layers, compared with when dust is assimilated. This is analyzed further in the next section.

### 5.3. Temperature and Dust Structure During the Onset of the MY34 GDS

We now compare the atmospheric temperature and dust structure between the analyses, the GCM ensemble, and MCS observations. Figures 11 and 12 show time-latitude sections for temperature and dust DSO at 21.6  $\mu\text{m}$ , at 30 Pa (where MCS dust concentrations are highest during the storm). These cover all latitudes starting before

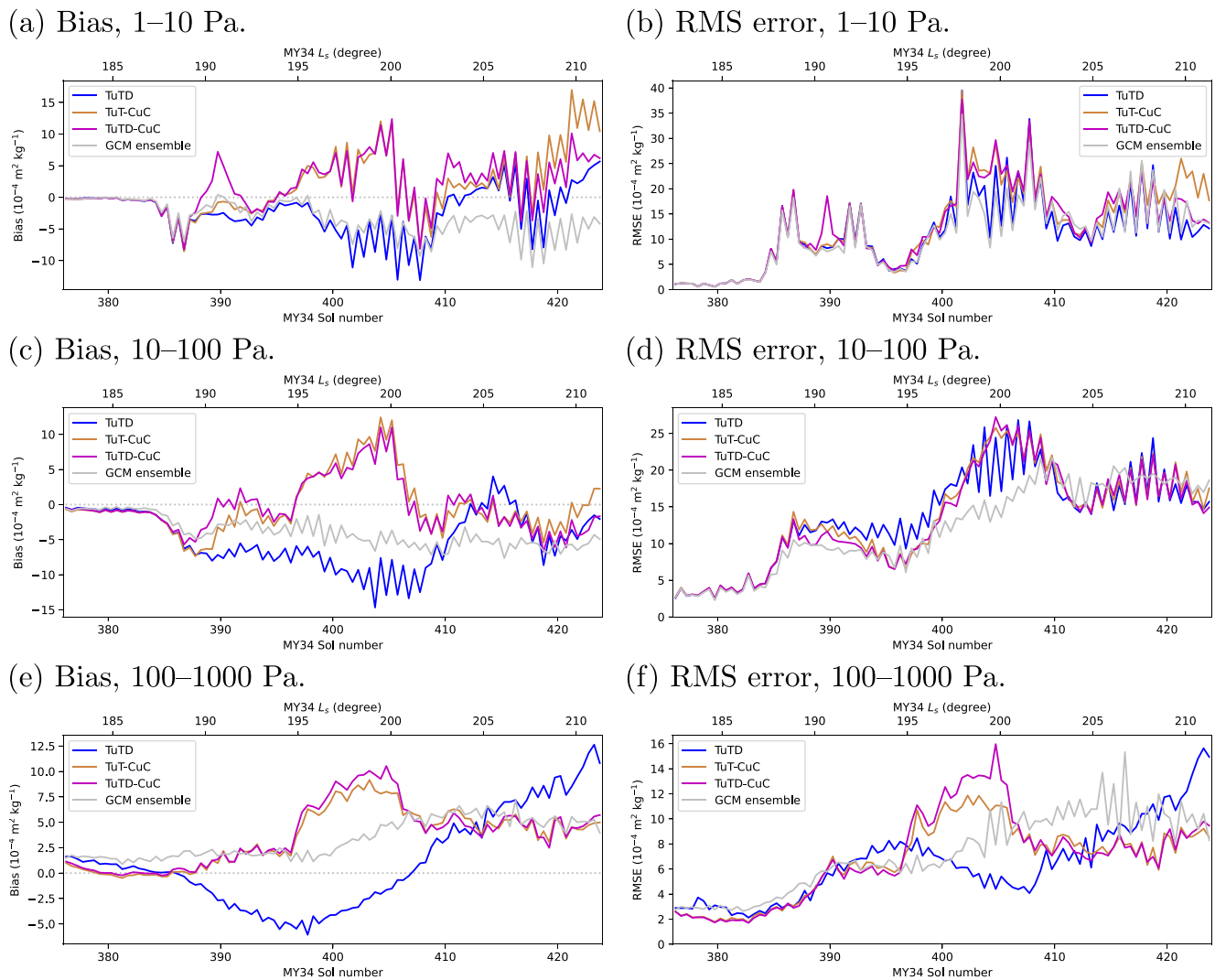


**Figure 10.** Same as Figure 9, but showing independent verification against Mars Climate Sounder extinction dust density-scaled opacity profiles.

the storm and ending just after its peak. Figure 13 shows vertical cross-sections of temperature at 3 p.m. and 3 a.m. local mean solar time (chosen because i.e., the observation time for MCS), and Figure 14 shows the same for dust DSO.

There is significant heating associated with the GDS, with equatorial temperatures rising from 180 to 225 K over this period (Figure 11). Assimilating dust observations significantly improves the temperature analysis with respect to the independent MCS observations. When no dust observations are assimilated (Figure 11a) the temperature change due to the storm over this  $L_s$  range is somewhat slower than observed by MCS (although 225 K is reached by the end). But when CDODs are assimilated (Figures 11b and 11c) the change in temperature better matches the MCS observations. Other details also match better, such as the hemispheric asymmetry at the peak of the storm. The differences between the case with and without the TuD step are small, but TuTD-CuD gives marginally better results, particularly for sols 391–396 (Figure 11c).

We note that, during the latter part of the onset of the storm (sols 397–410), the TIRVIM observations are at 8–10 a.m./p.m. local time (Figures 2e and 2f), 5–7 hr out of phase with the MCS observations at 3 a.m./p.m. This means that, during this part of the assimilation, the GCM integrates the atmospheric state for several hours between being constrained by TIRVIM observations and the 3 p.m. local time displayed in Figure 11. Hence large temperature differences between the different configurations during that period may also be because the

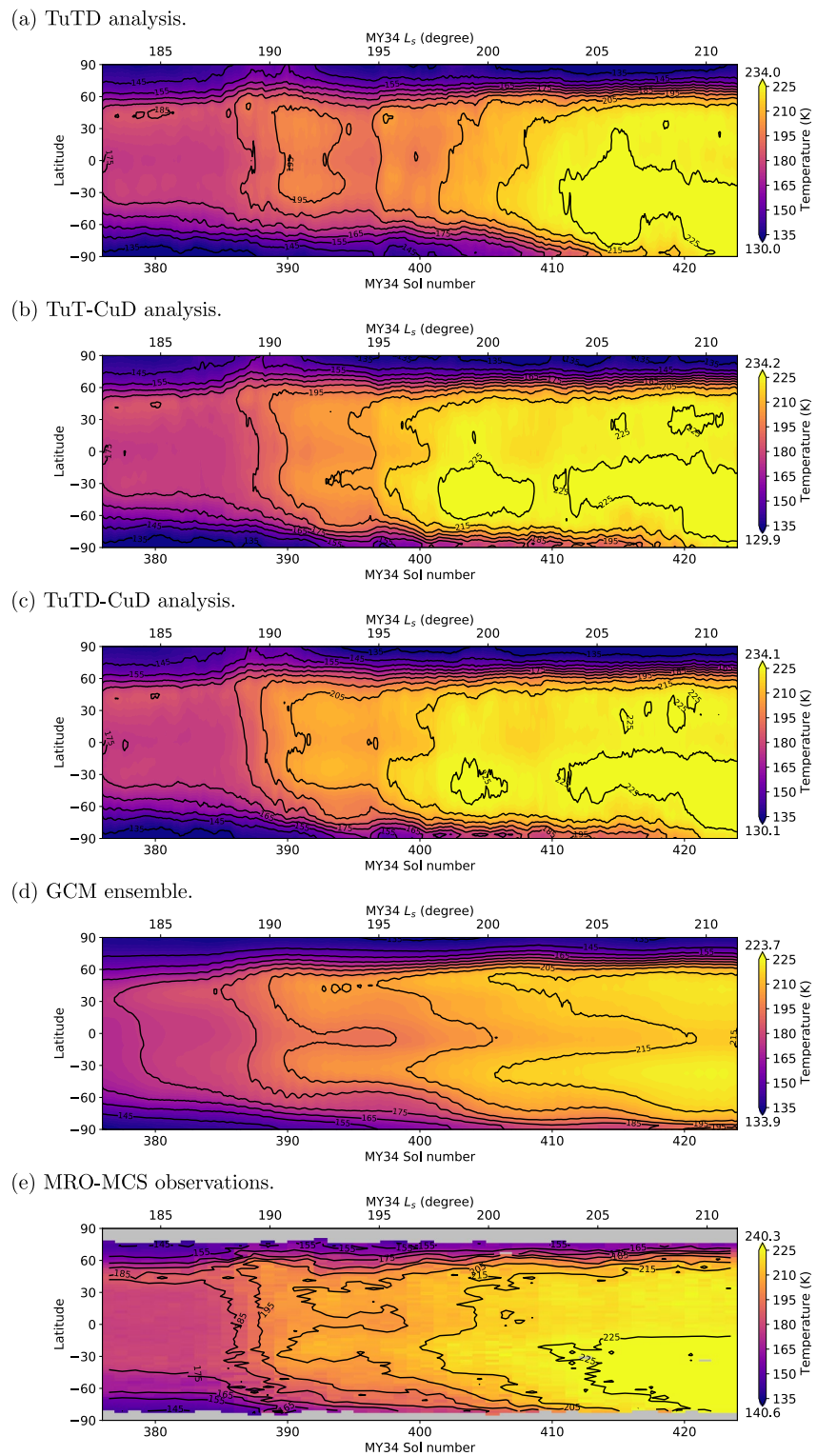


**Figure 11.** Time-latitude sections showing analysis temperature at 30 Pa at 3 pm local mean solar time (LMST). (a) TuTD analysis; (b) TuT-CuD analysis; (c) TuTD-CuD analysis; (d) GCM ensemble; and (e) Mars Reconnaissance Orbiter (MRO)-Mars Climate Sounder (MCS) observations. Data are smoothed using a 1-sol running mean. Gray indicates missing data. Line contours are every 10 K. MCS observations between 2 and 4 p.m. LMST are used; analyses are interpolated to 3 p.m. LMST. Maxima and minima are shown above and below the color bar.

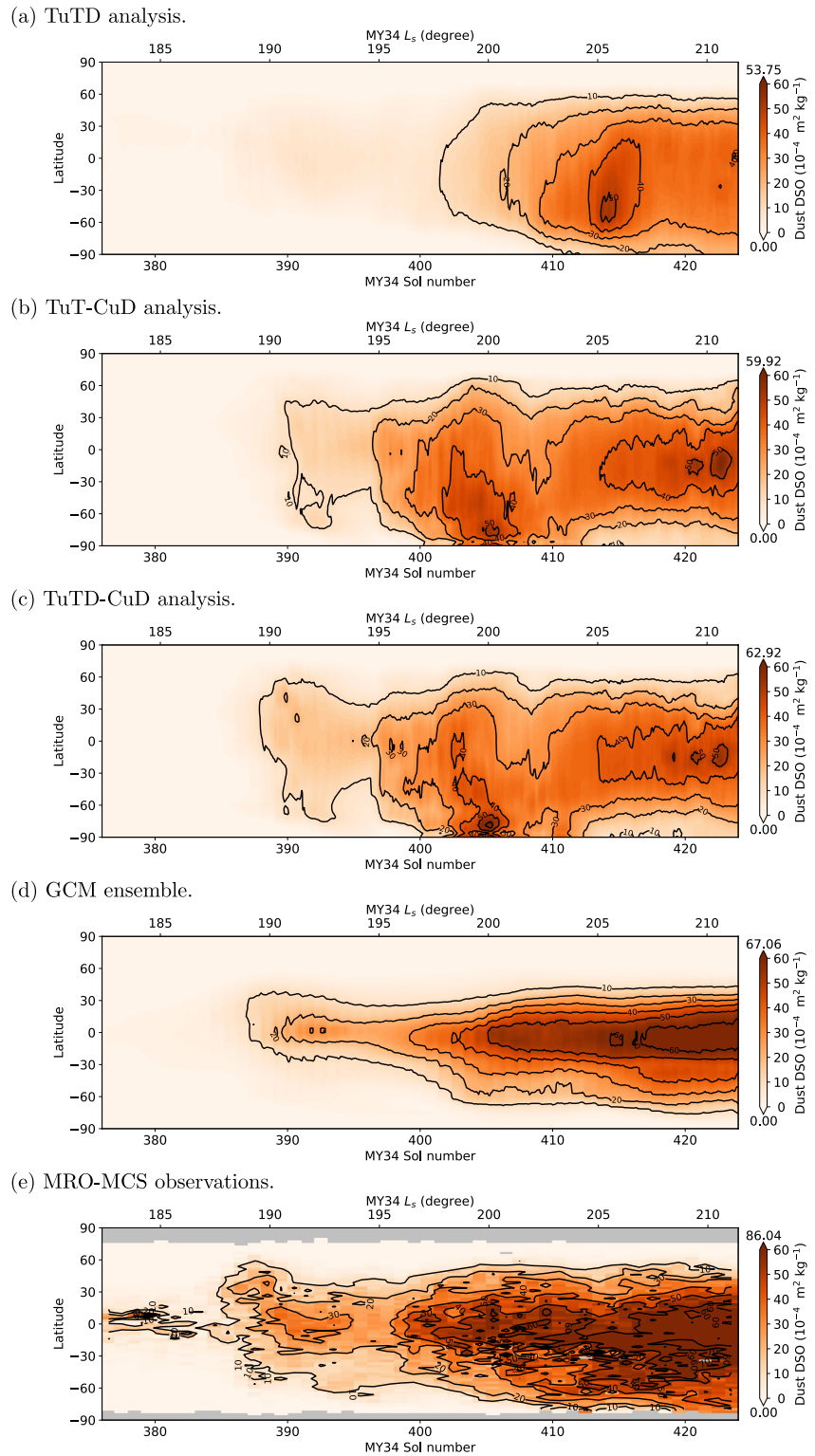


**Figure 12.** Same as Figure 11, but showing time-latitude sections for dust density-scaled opacity at 21.6  $\mu\text{m}$  at 30 Pa. Line contours are every  $10 \times 10^{-4} \text{ m}^2 \text{ kg}^{-1}$ .

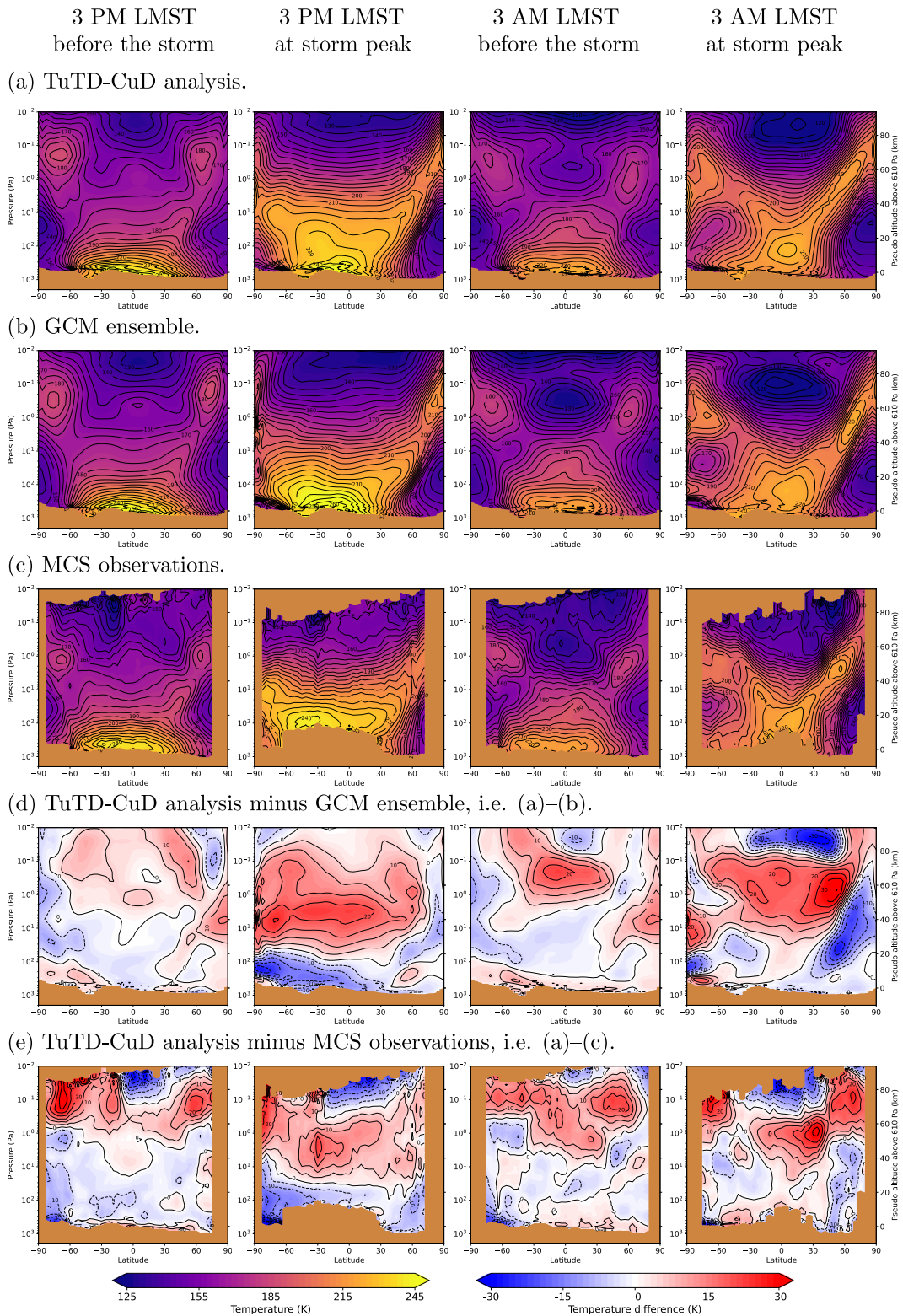


**Figure 13.** Temperature cross-sections at 3 p.m. and 3 a.m. local mean solar time. (a) TuTD-CuD analysis; (b) Global Climate Model (GCM) ensemble; (c) Mars Climate Sounder (MCS) observations (up to 1 hr either side of the target local time); (d) TuTD-CuD minus GCM ensemble; and (e) TuTD-CuD minus MCS observations. Columns 1–2 show 3 p.m., and columns 3–4 show 3 a.m. Columns 1 and 3 show before the storm, averaged over sols 380–384, and columns 2 and 4 show the peak of the storm, averaged over sols 416–420. The right vertical axis shows the pseudo-altitude above 610 Pa. Line contours are spaced every 5 K. Flat brown areas show missing data (either below the surface, or where there are no MCS observations).

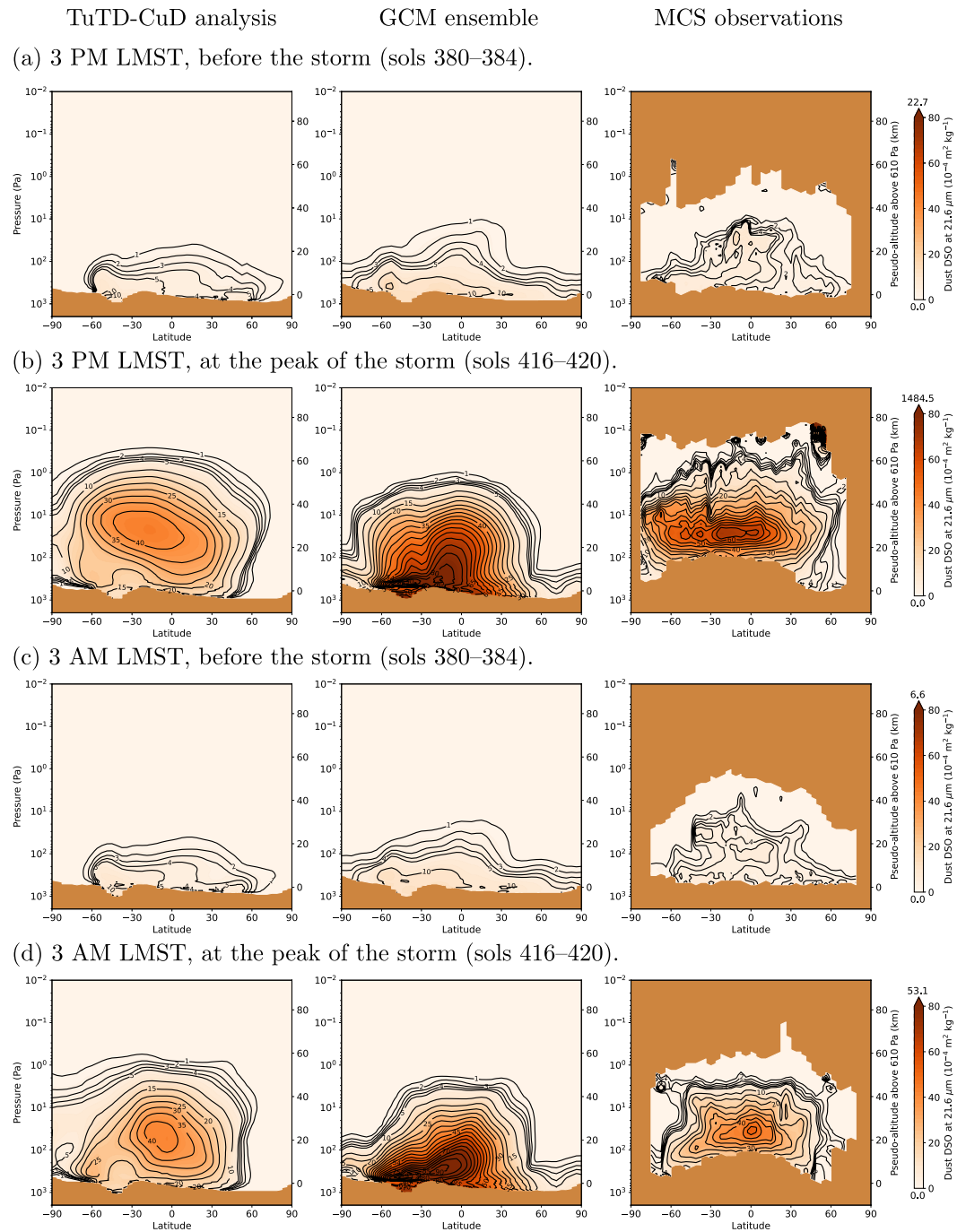


**Figure 14.** Same as Figure 13, but showing dust density-scaled opacity at 21.6  $\mu\text{m}$  at 3 p.m. and 3 a.m. local mean solar time. Line contours are spaced every  $10^{-4} \text{ m}^2 \text{ kg}^{-1}$  from  $1-4 \times 10^{-4} \text{ m}^2 \text{ kg}^{-1}$ , and then every  $5 \times 10^{-4} \text{ m}^2 \text{ kg}^{-1}$  thereafter.

atmospheric state is not constrained by observations near the MCS observation time. Equivalent figures to Figures 11a and 11b (not shown) at 9 a.m. LMST are closer together during sols 397–410.

The GCM ensemble captures the minimum at the equator around sol 395 better than the analyses, but overall the analyses match the MCS observations better. The former underestimates the atmospheric temperature at most latitudes, and does not fully reproduce the observed hemispheric asymmetry at the peak of the storm.

The temperature results at 3 a.m. are similar, although the differences between the GCM ensemble and the analyses are smaller. Time-latitude sections for 3 a.m. are shown in Figure S1 in Supporting Information S1.

The differences in dust DSO between the various configurations (Figure 12) are larger than for temperature. MCS observations show a peak in the dust DSO around  $60 \times 10^{-4} \text{ m}^2 \text{ kg}^{-1}$ . The GCM ensemble (Figure 12d), whose column abundance is constrained by MCS observations, matches the dust DSO reasonably well, at least in terms of its evolution during the onset of the storm up to the peak, although the distribution is more strongly concentrated at the equator than for the MCS observations.

The three analyses each contain overall less dust than do the MCS observations. The largest difference is between TuTD and the other two cases. For TuTD (Figure 12a), dust opacity increases slowly during the onset of the storm, and only begins to change rapidly close to its peak. The other two cases (Figures 12b and 12c) follow the increase in dust during the onset of the storm better, although neither reach the peak opacity measured by MCS at this pressure by the peak of the storm. None of the three analyses reproduce the short-lived peak at the equator between sols 389–393, but we note this partially coincides with a gap in the TIRVIM data. Nevertheless, it is clearly better to have assimilated the dust information directly, both in terms of the temperature analysis and the dust analysis.

The equivalent plots at 3 a.m., shown in Figure S2 in Supporting Information S1, show a more favorable comparison between the TuT-CuD/TuTD-CuD analyses and MCS observations. Both reach the peak dust opacity seen in MCS observations by the peak of the storm (which we note the GCM ensemble does not do at 3 a.m.). They also reasonably reproduce the growth in dust concentration from sol 397 onwards. Kleinböhl et al. (2020) discuss the significant diurnal variations of temperature and dust opacity in the MCS observations during the dust storm in some detail.

Figures 13 and 14 show vertical cross-sections of the temperature and dust DSO before and at the peak of the GDS. These figures show how well the analysis reproduces the vertical structure, compared with the GCM ensemble and MCS observed profiles. In these figures and hereafter we only use our “best case” assimilation TuTD-CuD, alongside the GCM ensemble.

Both the temperature and dust opacity increase significantly during the storm, during daytime and nighttime. Unfortunately it is not possible to compare directly with daytime MCS observations at the peak of the storm near the surface, as the high dust concentration prevents a reliable retrieval of both temperature and dust (Figure 13c, second column). The analysis and GCM ensemble both have a temperature maximum of 250–260 K close to the surface during the daytime at the peak of the storm. The maximum MCS temperature is at about 100 Pa, and appears to be a local maximum.

The main difference between the analysis and GCM ensemble (Figure 13d), and the analysis and MCS observations (Figure 13e), both at daytime and nighttime, before the storm and at the peak of the storm, occurs above about 40–60 km altitude. The assimilated TIRVIM observations typically go up to about 1 Pa, so above this any differences are due to the GCM's response to assimilated data rather than being constrained directly by observations. The analysis is typically warmer than the GCM ensemble and the MCS observations there.

Below this level, where there are TIRVIM observations, the analysis generally agrees with MCS observations within 5 K, except during daytime at the peak of the storm (Figure 13e, second column), where the differences go above 10 K in places. During the daytime the analysis temperatures below 50 Pa are generally lower than the MCS observations. This may be because at low altitudes during daytime the MCS observations are biased warm compared with TIRVIM due to a lack of retrievals in cloudy regions; see Guerlet et al. (2022, Figure 19). In northern midlatitudes the observed profiles do reach the ground, and the analysis reasonably reproduces the observed meridional temperature gradient in the northern hemisphere. In the southern hemisphere the near-surface analysis is cooler than MCS observations, so the meridional temperature gradient is steeper than observed.

Both the analysis and the GCM ensemble reproduce the tongue of warm air in the middle atmosphere at northern hemisphere midlatitudes, which appears at the peak of the storm. At the peak of the storm, the analysis reproduces the nighttime local temperature maximum around 100 Pa that appears in the MCS observations better than does the GCM ensemble. The analysis and GCM ensemble have quite different temperature structures near the top of the domain near the equator, with the local temperature minimum in the GCM ensemble being about a decade

in pressure below where it is in the analysis. The location of the polar inversion layer is also higher in the analysis than in the MCS observations, at all four times shown in Figure 13.

As in the time-latitude sections, there is a larger difference between the analysis and the GCM ensemble in the dust opacity cross-sections (Figure 14) than in temperature (Figure 13). Before the storm, the amount of dust peaks around  $5 \times 10^{-4} \text{ m}^2 \text{ kg}^{-1}$  in the analysis and  $10 \times 10^{-4} \text{ m}^2 \text{ kg}^{-1}$  in the GCM ensemble, with little diurnal variation (Figures 14a and 14c). The MCS observations peak at about  $5 \times 10^{-4} \text{ m}^2 \text{ kg}^{-1}$ , but the main difference is that the dust is more vertically extended in the observations, with a clear “detached dust layer” peak near the equator during the night-time around 100 Pa of about  $5 \times 10^{-4} \text{ m}^2 \text{ kg}^{-1}$ , which is not visible in either the analysis or the GCM ensemble.

At the peak of the storm there are larger differences between daytime (Figure 14b) and nighttime (Figure 14d), as well as between the analysis, GCM ensemble, and MCS observations (Figure 14, different columns). In general, the GCM ensemble contains significantly more dust than either the analysis or the MCS observations. The peak in the GCM ensemble is close to the ground in the southern hemisphere, about  $90 \times 10^{-4} \text{ m}^2 \text{ kg}^{-1}$  at both 3 p.m. and 3 a.m., while the MCS observations peak at about 30 Pa, with maxima around  $60 \times 10^{-4} \text{ m}^2 \text{ kg}^{-1}$  at 3 p.m. and a concentrated peak of  $50 \times 10^{-4} \text{ m}^2 \text{ kg}^{-1}$  at 3 a.m.

The analysis reproduces the vertical and latitudinal distribution of dust opacities significantly better than does the GCM ensemble. In particular, it very clearly contains a detached dust layer at both 3 p.m. and 3 a.m., with a broad peak between 10 and 100 Pa, as seen in the MCS observations, while the GCM ensemble peaks near the surface (although note not exactly at the surface). The peak dust DSO in the analysis is about  $40 \times 10^{-4} \text{ m}^2 \text{ kg}^{-1}$  at both 3 p.m. and 3 a.m. During the daytime this is an underestimate, as the dust opacity peak in the MCS observations is above  $50 \times 10^{-4} \text{ m}^2 \text{ kg}^{-1}$  between  $60^\circ\text{S}$  and  $20^\circ\text{N}$ . During nighttime the MCS observations peak at  $50 \times 10^{-4} \text{ m}^2 \text{ kg}^{-1}$  near the equator. However, there is significantly less dust than during the daytime, with the opacity above  $40 \times 10^{-4} \text{ m}^2 \text{ kg}^{-1}$  between  $20^\circ\text{S}$  and  $20^\circ\text{N}$ . This distribution is matched well by the analysis dust opacity at this time, which is above  $40 \times 10^{-4} \text{ m}^2 \text{ kg}^{-1}$  between  $20^\circ\text{S}$  and the equator.

#### 5.4. Wind Structure Retrieved by Assimilation

Having demonstrated that our reanalysis state fits the independent MCS observations reasonably well, we now turn to wind, a quantity that is not observed but which is retrieved by the assimilation. This is one of the main strengths of the data assimilation process.

Figures 15 and 16 show the meridional mass stream function and zonal velocity at 3 p.m. and 3 a.m. local mean solar time averaged over two time periods before the storm and at its peak. Before the storm, the daytime overturning circulation (Figures 15a and 15b) shows a Hadley cell covering the whole of each hemisphere. There is a weak counter-rotating cell higher than 10 Pa, which only appears in the GCM ensemble. The study period is close to the autumnal equinox, so the Hadley cell is approximately symmetric about the equator. During nighttime (Figures 15c and 15d) the overturning circulation is reversed, with the descending branch of the main overturning cell at the equator, with a weaker thermally direct cell between 1 and 10 Pa. The meridional overturning circulation is generally weaker in the analysis than in the GCM ensemble.

The overturning circulation strengthens during the daytime as the storm progresses, and extends higher into the atmosphere, significantly strengthening the overturning circulation aloft. The thermally indirect cell present in the GCM ensemble disappears, leaving a single Hadley cell spanning the whole model domain from the surface to 100 km pseudo-altitude. We note that, under normal circumstances, the northern hemisphere cell expands at this time of year, rather than the southern hemisphere cell (Barnes et al., 2017, Figure 9.10). Close to the surface, the southern hemisphere cell extends about  $40^\circ$  into the northern hemisphere. At nighttime the circulation changes considerably. The symmetric Hadley cells are severely disrupted, and a cross-equatorial cell develops which covers most latitudes with a weak Hadley circulation in the northern polar region.

The zonal velocity during the storm (Figure 16) is noticeably asymmetric about the equator, both during daytime and nighttime. Like the meridional overturning circulation, this change is more profound during nighttime. Before the storm there are prograde jets in both hemispheres with a retrograde jet above 1 Pa at low latitudes, and these jets are slightly weaker at 3 a.m. By the peak of the storm, the equatorial retrograde jet and the prograde northern hemisphere jet increase in speed by about 25 and  $75 \text{ m s}^{-1}$  respectively, while the southern hemisphere



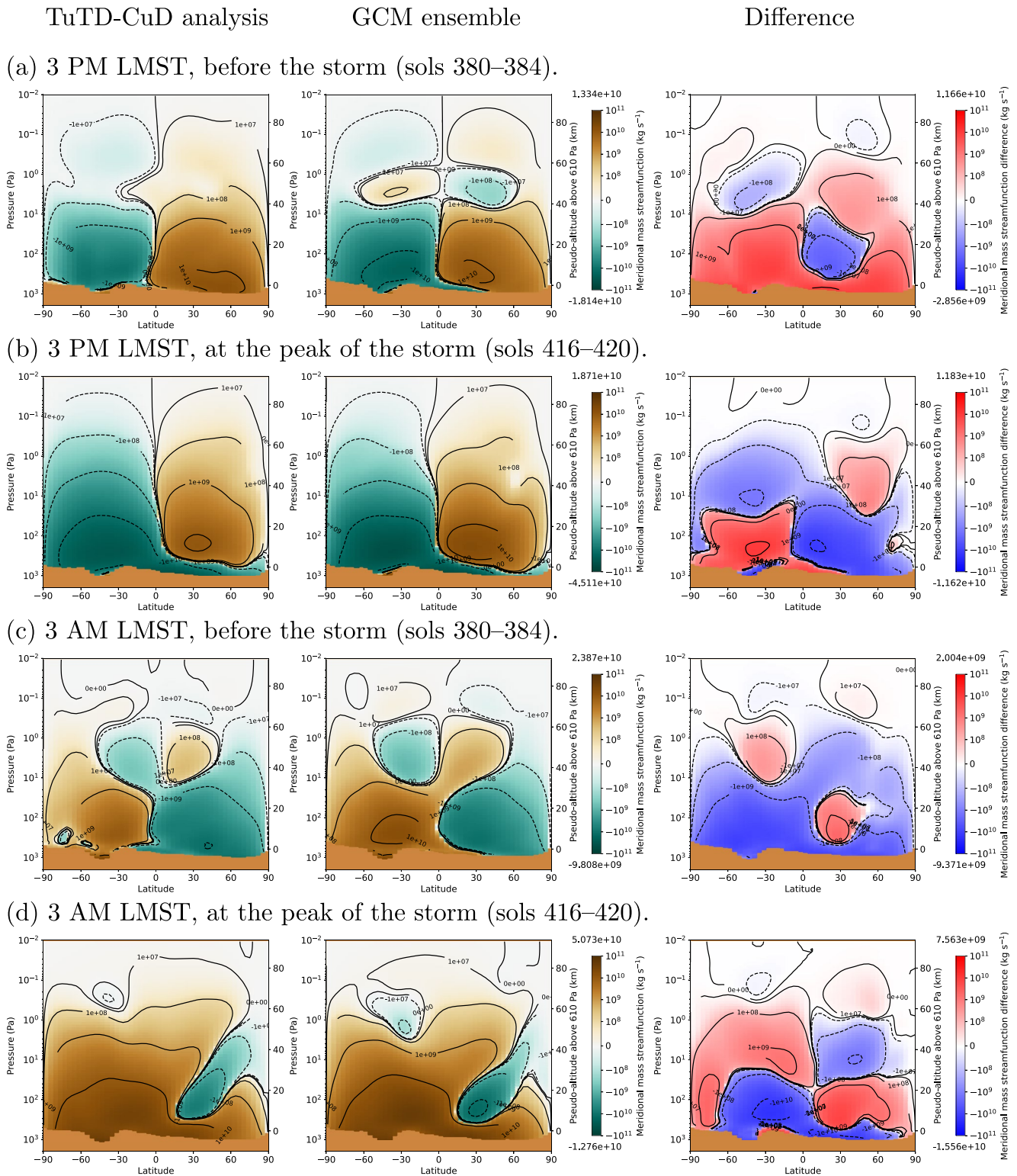


**Figure 15.** Same as Figure 13, but showing the meridional mass streamfunction at 3 p.m. and 3 a.m. local mean solar time. The right hand column shows the difference between the analysis and Global Climate Model (GCM) ensemble (analysis—GCM). In the left two columns brown is clockwise motion and blue is anticlockwise motion. In the right column red means more clockwise, and blue means more anticlockwise. Line contours are spaced every factor of 10 between  $10^8$  and  $10^{11}$   $\text{kg s}^{-1}$ .

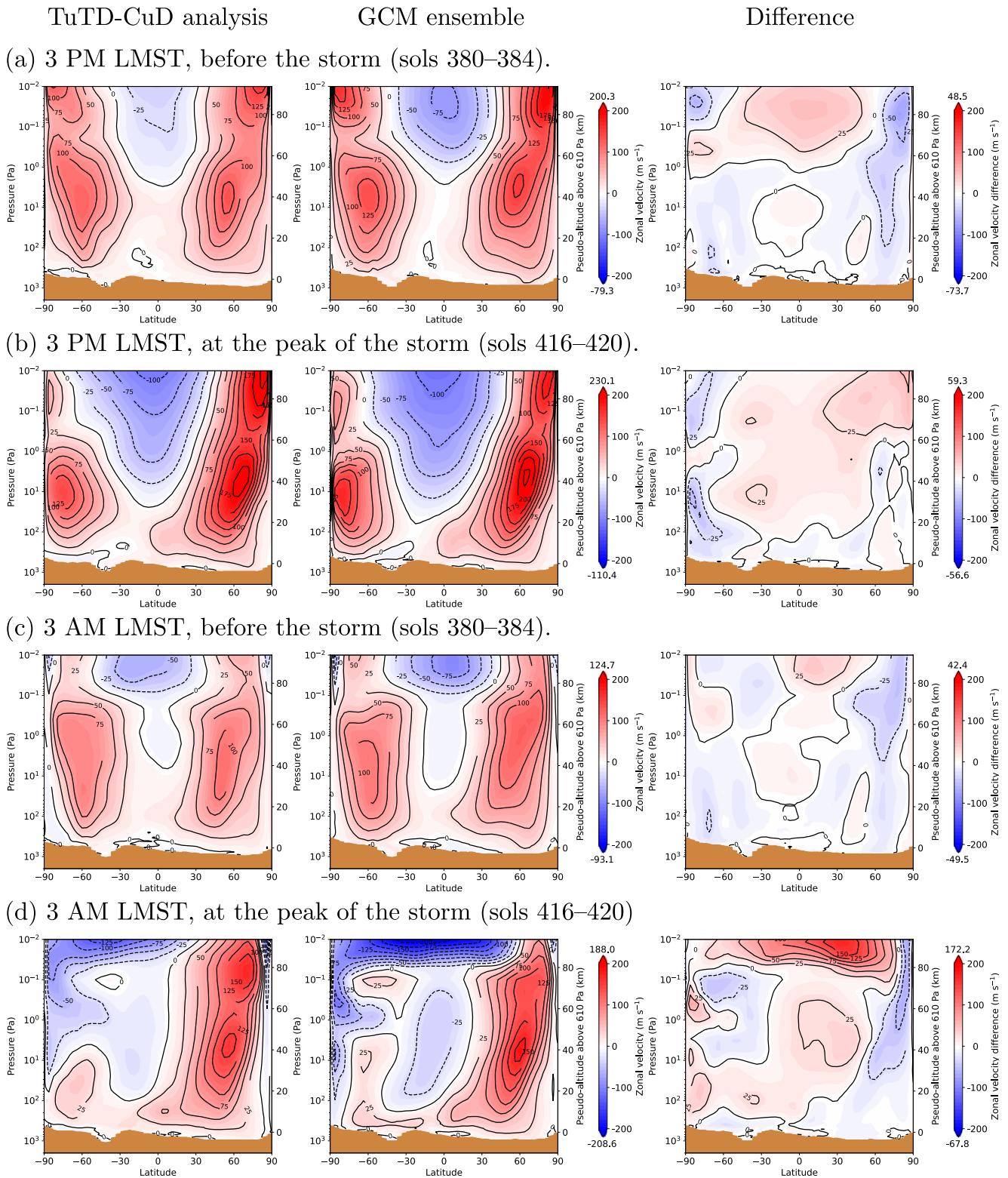


Figure 16. Same as Figure 15, but showing the zonal velocity at 3 p.m. and 3 a.m. local mean solar time. Line contours are spaced every 25 m s<sup>-1</sup>.

prograde jet remains approximately the same speed but its vertical extent shrinks, becoming a more focused jet around 75°S/10 Pa. During nighttime, the northern prograde jet strengthens by about 50 m s<sup>-1</sup>, but the southern prograde jet weakens significantly by about 75 m s<sup>-1</sup>, almost disappearing. At the peak of the storm, the two prograde jets differ in speed by 125 m s<sup>-1</sup>. The strong strengthening of the northern hemisphere jet at both 3 p.m. and 3 a.m. is consistent with the steepening of the latitudinal temperature gradient near 60°N at the peak of the storm (Figures 13b–13d), via thermal wind balance. A similar argument explains the weakening of the southern prograde jet: the temperature contours are flattened in the southern hemisphere around 10 Pa (Figures 13a and 13b).

Differences between the analysis and the GCM ensemble are relatively small compared with the magnitude of the jets, with typical differences up to  $\pm 25$  m s<sup>-1</sup> over most of the domain. The analysis winds are typically more eastward at lower latitudes than the GCM ensemble, in particular above 10 Pa, and they are typically more westward at higher latitudes.

### 5.5. Diurnal Cycle and Thermal Tides

One of the reasons for the design of the ExoMars TGO orbit is that it samples the Martian atmosphere at different local times of day. In this section we present how this affects the analysis, and analyze how the diurnal cycle changes during the GDS. Assimilation constrains the atmosphere at particular local times, and then the forecast model transfers that information to other local times during model integration, further constraining the atmospheric structure at local times that were not observed. For sols 380–384 the bulk of the TIRVIM observations are at 1–2 a.m./p.m., and for sols 416–420 they are at 5–6 a.m./p.m. (Figures 2e and 2f). First, we look at the diurnal cycle in two different ways (Figures 17 and 18) and then analyze the migrating Sun-synchronous tide modes (Figures 19 and 20). Note that where MCS observations are not part of the analysis, we do our computations in LTST, as that is more dynamically relevant than LMST, and it is the local time used in the Mars PCM.

Figure 17 shows the temperature diurnal cycle averaged over two different latitude bands before and at the peak of the GDS. We interpolated the analysis and the GCM ensemble to fixed pressure levels, and then interpolated to each local time in 1-hr steps. We then averaged the temperature at each pressure and local time over latitude and sol ranges. This was done at 60–65° S (to match Figure 4.13 of M. D. Smith et al. (2017)), and over a latitude band at the equator.

There is a significant difference between the diurnal cycle before and at the peak of the storm. At 60°–65°S (Figures 17a and 17b) the range of temperatures at all altitudes significantly increases with the peak to peak diurnal variability increasing from about 10 K at 30 Pa before the storm to about 60 K at the peak of the storm. In the middle atmosphere (0.1–1 Pa), the 12-hr oscillation is overwhelmed by a 24-hr oscillation that peaks between 3 and 6 a.m.

The main difference between the analysis and GCM ensemble is in the lower atmosphere temperature maximum around 6 p.m. In the analysis this is concentrated in the local time direction between 6 and 8 p.m., and is extended in the pressure direction up to about 10 Pa. In the GCM ensemble the peak is concentrated closer to the ground, up to about 100 Pa, but spans a longer range of local times. The peak during the night time in the lower atmosphere is quite similar in the analysis and the GCM ensemble.

At the equator (Figures 17c and 17d), we also see the 12-hr oscillation in the upper part of the domain weaken. In the analysis the peak around 12 p.m. between 0.1 and 1 Pa almost completely disappears during the peak of the storm, while in the GCM ensemble it is still distinguishable. Lower in the atmosphere the 12-hr oscillation is strengthened both in the analysis and the GCM ensemble at the peak of the storm, and the 24-hr oscillation is less clear, although in the analysis the 12-hr oscillation is dominant while in the GCM ensemble the 24-hr oscillation is dominant.

We can compare diurnal variations in our analysis against independent MCS observations by measuring the temperature differences between 3 p.m. and 3 a.m. This comparison can only be made between those two local times, but it is one aspect of the diurnal cycle that can be compared directly with observations. This is shown in Figure 18. Both the analysis and the GCM ensemble reproduce most basic aspects of the MCS observations, both before the storm and at its peak. Differences between 3 p.m. and 3 a.m. temperatures are generally smaller in the analysis compared with the MCS observations. The GCM ensemble matches the MCS observations reasonably

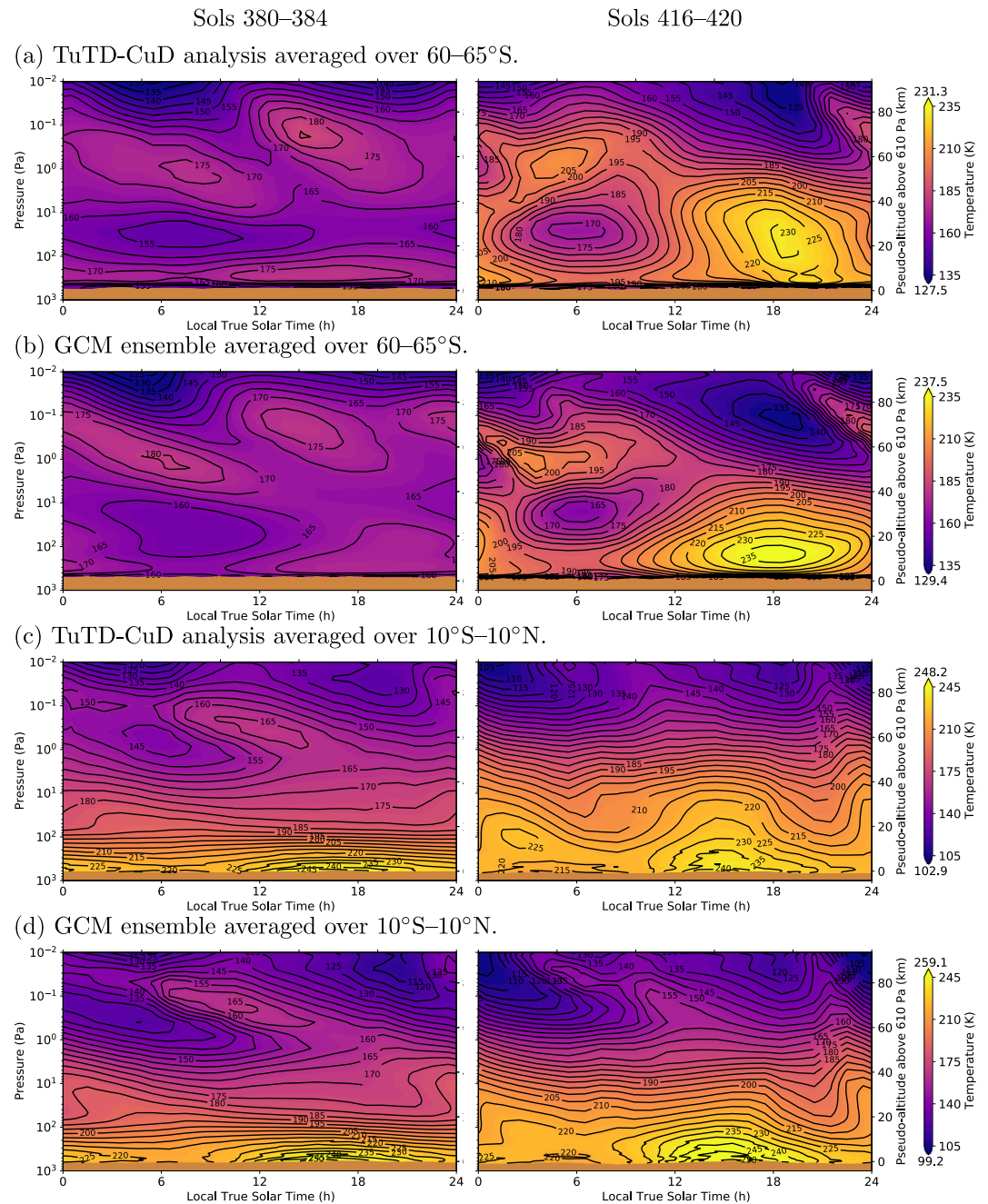


**Figure 17.** Vertical temperature structure against local true solar time. The left column shows a mean over MY34 sols 380–384 (before the storm) and the right column shows sols 416–420 (at the peak of the storm). The color scale is the same for both columns, but note the color scales for (a and b) and (c and d) are slightly different. From top: (a) TuTD-CuD analysis averaged over 60°–65°S; (b) Global Climate Model (GCM) ensemble for 60°–65°S; (c) TuTD-CuD analysis for 10°S–10°N; and (d) GCM ensemble for 10°S–10°N. Numbers above and below the color bars indicate the minimum and maximum temperature for sols 416–420, and line contours are every 5 K.

well before the storm, while at the peak of the storm it tends to overestimate differences in the upper atmosphere and underestimate them in the lower atmosphere. The general position of the peaks and troughs in the MCS observations are reproduced well by both the analysis and the GCM ensemble.

At the peak of the storm the quadrupole structure disappears and is replaced at mid-to-high latitudes by a strong positive anomaly in the lower atmosphere and a strong negative anomaly in the middle atmosphere. Near the

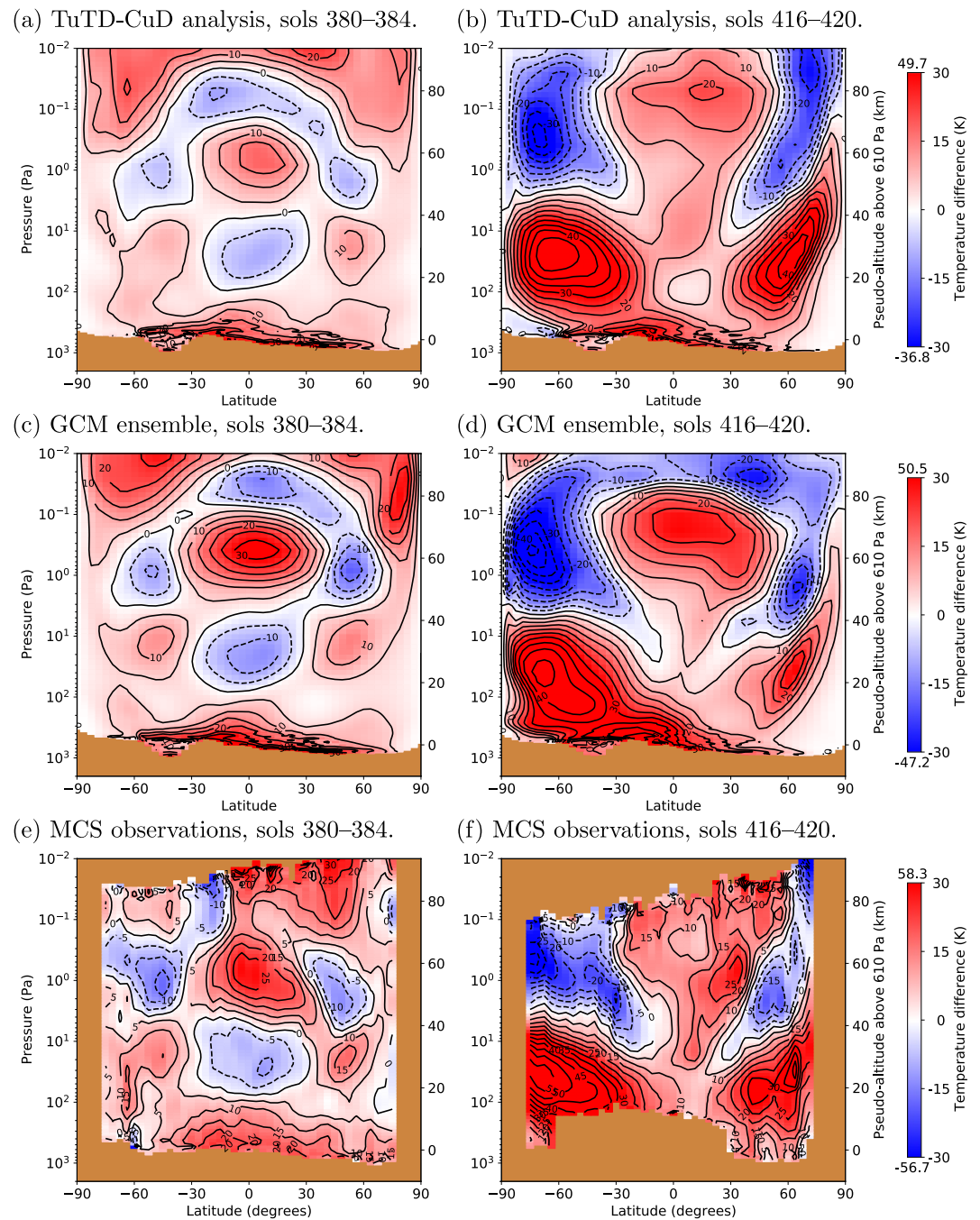


**Figure 18.** Difference between 3 p.m. and 3 a.m. temperatures (local mean solar time) for (a and b) TuTD-CuD analysis; (c and d) Global Climate Model (GCM) ensemble; and (e and f) Mars Climate Sounder (MCS) observations (using observations between LMST 2–4 a.m./p.m.). The left column (a, c, e) shows sols 380–384, before the storm, and the right column (b, d, f) shows sols 416–420, at the peak of the storm. Brown is missing data (either below the surface, or not observed). Numbers above and below the color bars indicate the minimum and maximum values for sols 416–420. Line contours are at 5 K intervals.

equator the temperature difference is small in the lower atmosphere and increases significantly in the middle atmosphere. In most areas the analysis is closer than the GCM ensemble to the MCS observations. In the northern hemisphere the analysis better matches the anomaly magnitudes and vertical structure. In the equatorial region the positive anomaly in the GCM ensemble is more compact than in the MCS observations. Because the MCS

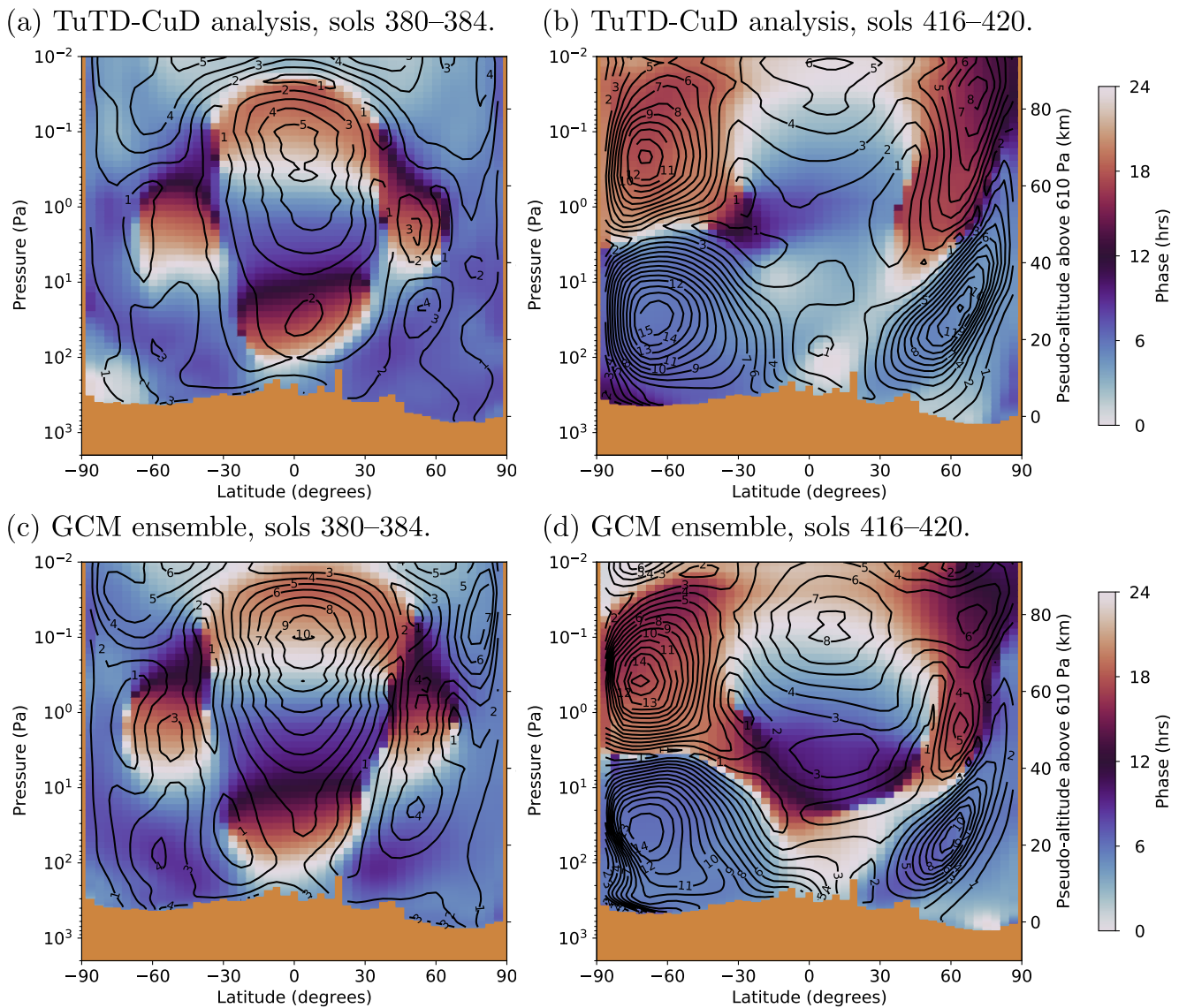


**Figure 19.** Amplitude and phase of the sun-synchronous migrating diurnal tide  $S_1$ . (a and b) TuTD-CuD analysis; and (c and d) Global Climate Model (GCM) ensemble. The left column (a and c) is for sols 380–384, and the right column (b and d) is for sols 416–420. Filled color contours show the phase (scaled to local true solar time between 0 and 24 hr), and line contours show the amplitude (spaced at 1 K intervals).

observations don't reach the ground, we cannot tell whether the analysis or GCM ensemble better matches reality near the ground in the southern hemisphere.

Figures 19 and 20 show the amplitude and phase of the westward-propagating Sun-synchronous migrating diurnal and semi-diurnal tides, respectively, before and at the peak of the storm. We interpolated the analysis and the GCM ensemble temperature fields to a fixed set of pressure coordinates. At each pressure and latitude point this gave temperature as a function of longitude and absolute time (over the 4-sol periods we have used throughout), which we then decomposed into its Fourier modes to give a two-dimensional spectrum as a function of longitudinal wavenumber and frequency. We then extracted the amplitude and phase of the period-(1 sol), wavenumber-(−1) mode, which is the westward-propagating Sun-synchronous migrating diurnal tide  $S_1$ ; and the period-(0.5 sol), wavenumber-(−2) mode, which is the equivalent semi-diurnal tide mode  $S_2$ . The phase is expressed in terms of hours (0–24 for the diurnal tide and 0–12 for the semi-diurnal tide).

Before the storm the spatial patterns of the diurnal tide (Figure 19) are similar to those in Figure 18. The phase data exhibit a quadrupole structure before the storm, and at the peak of the storm the vast majority of the power

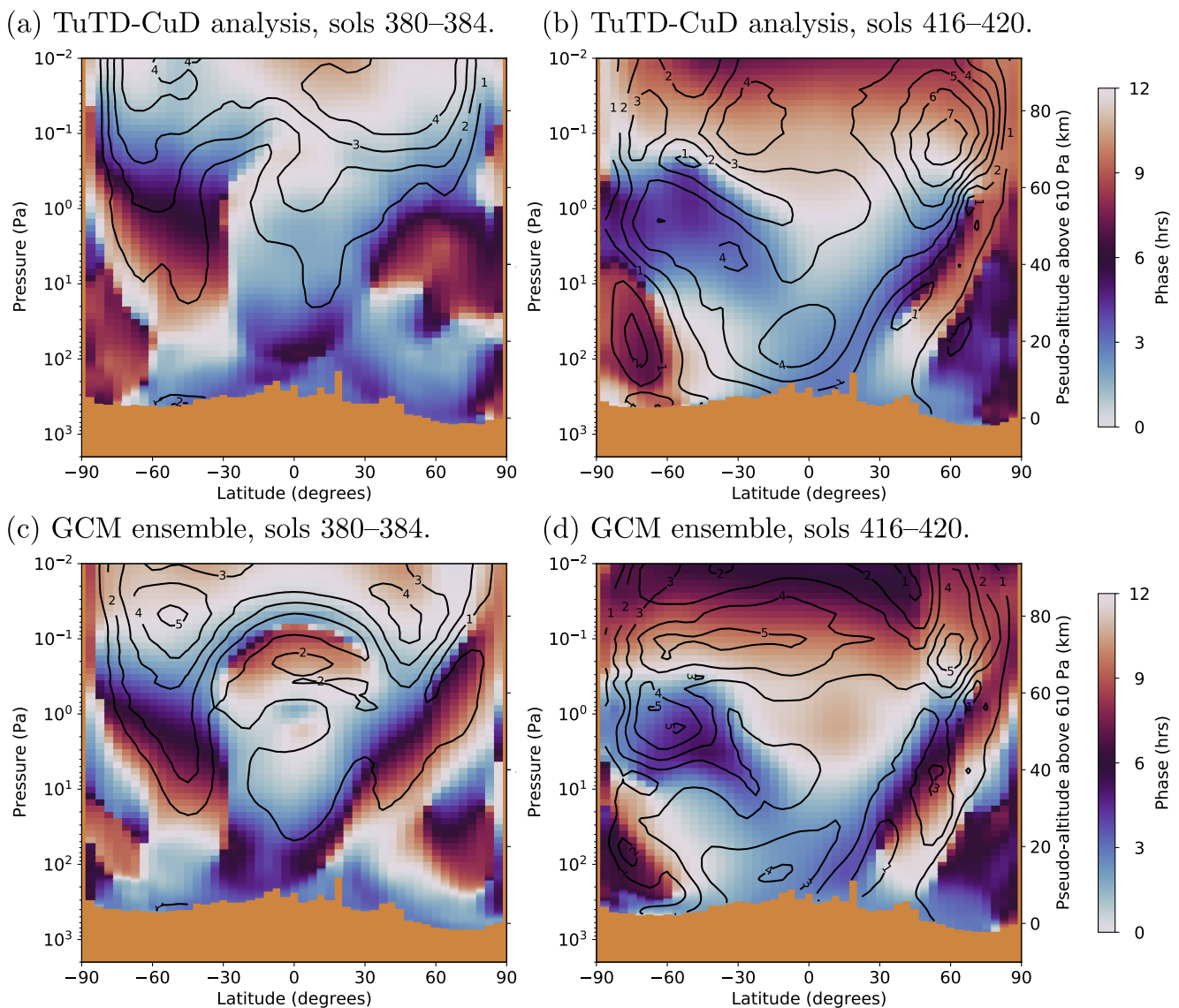


**Figure 20.** Same as Figure 19, but showing the amplitude and phase of the sun-synchronous migrating semi-diurnal tide  $S_2$ . In this case the filled color contours show the phase scaled to local true solar time between 0 and 12 hr.

in the diurnal tide is at mid- and high latitudes, with a weaker diurnal tide at the equator. This is consistent with what we showed in Figure 17. Before the storm, the diurnal tide has a maximum amplitude near the equator of about 5 K in the analysis and 10 K in the GCM ensemble (note that Figure 18 shows the difference between two local times separated by 12 hr, not a wave amplitude). This difference suggests that the amplitude of the diurnal tide is overestimated in the GCM ensemble.

At the peak of the storm the diurnal tide amplitudes in the GCM ensemble and analysis are closer, although near the equator the analysis is again weaker than the GCM ensemble, particularly at high altitudes. The analysis peaks at about 6 K right at the top of the domain, while the GCM ensemble peaks at 8 K around 0.1 Pa. At mid and high latitudes, however, the analysis and the GCM ensemble agree within about 1 K. One difference between the analysis and the GCM ensemble at the peak of the storm is the phase of the diurnal tide near the equator below 1 Pa. In the analysis this phase is 3–9 hr, whereas in the GCM ensemble it is 9–24 hr, a significant phase shift.

Before the storm the amplitude of the semi-diurnal tide (Figure 20) is small in the lower atmosphere, increasing to about 4 K in the upper parts of the domain. The amplitude is largely independent of latitude in the analysis, but there is a slightly larger amplitude and one peak in each hemisphere around 50°N/S in the GCM ensemble. We

may compare these figures before the storm directly with equivalent figures in Kleinböhl et al. (2013). Before the storm the general pattern is similar except for the phase near the equator. The phase generally increases downwards, starting around 0 hr at the top of the domain, and reaching 6 hr around 1 Pa. In Kleinböhl et al. (2013) this is only a weak function of latitude, but in our analysis (Figure 20a, left) the phase of the semi-diurnal tide is 0–3 hr throughout most of the column, while in the GCM ensemble it displays the full range of phases, but goes though 6 hr much higher in the atmosphere than at higher latitudes.

At the peak of the storm the amplitude of the semi-diurnal tide increases at all altitude and latitudes, particularly near the surface, which increases in the analysis from less than 1 K to about 4 K. In the upper part of the domain the amplitude increases from 4 K to about 7 K at 0.1 Pa around 60°N. Again the amplitudes in the analysis are generally smaller than in the GCM ensemble, but not by much.

### 5.6. Verification Against Independent Surface Pressure Observations From Curiosity-REMS

The final verification of our analysis is to compare surface pressures with high time cadence measurements taken by the Mars Science Laboratory Curiosity rover Rover Environmental Monitoring Station (REMS). We interpolated the analysis surface pressure field from the GCM grid to Curiosity's longitude and latitude before the storm (sols 380–384) and at the peak of the storm (sols 416–420). We then corrected the surface pressure to account for the difference in surface elevation between the GCM grid and Curiosity. We used Mars Orbital Laser Altimeter (MOLA) data with 32 points per degree (D. E. Smith et al., 2001) to obtain the altitude of the Curiosity rover, interpolating the MOLA surface elevation to Curiosity's location at each time it made a pressure measurement during these two periods. We corrected the analysis surface pressure assuming hydrostatic balance and a pressure scale height based on the temperature at 1 km pseudo-altitude (Spiga et al., 2007). The correction factor is

$$p_{\text{corrected}} = p_{\text{original}} \exp\left(-\frac{z_{\text{Curiosity}} - z_{\text{GCM}}}{H}\right) \quad (9)$$

where  $H = RT/g$  is the scale height. Because Curiosity is deep within Gale Crater, which is not resolved by the Mars PCM, the typical change in elevation from the GCM grid to Curiosity's location was an enormous  $-2,720$  m, typically  $+160$  Pa.

There are uncertainties associated with the finite resolution of the MOLA grid (about 2 km), and we also assume that errors due to using Curiosity's location in the rover landing frame of reference (which is inclined to the direction of gravity by about 3°) are small. However, our estimated uncertainty due to these assumptions is smaller than the uncertainty in the pressure measurements themselves (5.8 Pa).

Figure 21 shows surface pressure time series and diurnal cycles at the Curiosity rover location over two 4-sol periods before and at the peak of the storm, for the GCM ensemble and our best-case assimilation (TuTD-CuD). Both the analysis and the GCM ensemble generally fit the measured Curiosity observations well. For the analysis, the match to the time series at the peak of the storm is particularly good, falling within the Curiosity measurement uncertainty. Given that we are down-sampling a climate resolution model (which does not resolve Gale Crater) with grid boxes approximately  $300 \text{ km} \times 200 \text{ km}$  to a single location within the crater, and then correcting the surface pressure for a difference in surface elevation close to 3 km, a mean error close to 10 Pa is remarkable.

The surface pressure rises during the storm by about 50 Pa, and the diurnal mode becomes stronger, with the peak-to-peak diurnal variation increasing from 80 to 120 Pa. The analysis is closer to the Curiosity observations than the GCM ensemble, reflecting the additional constraints on surface pressure from the assimilated temperatures. The analysis is better both in its absolute match to the Curiosity time series, and in how well the diurnal cycle is reproduced, both before and at the peak of the storm. The GCM ensemble overestimates the absolute pressure, and overestimates the peak-to-peak diurnal variability, compared with the analysis and the Curiosity measurements. This is reflected in the mean and RMS errors, which are significantly smaller for the analysis than for the GCM ensemble: about 50% before the storm and about 70% at the peak of the storm. Only between 2 and 7 a.m. does the analysis poorly track the diurnal surface pressure cycle at the Curiosity location at the peak of the storm, where it overestimates the observations. The same is seen in the GCM ensemble, although the error is larger. This is most likely due to mesoscale meteorology specific to Gale Crater, which is not accounted for in the model (see e.g., Raffkin et al., 2017 for a review). Our analysis' good agreement with observations, despite the



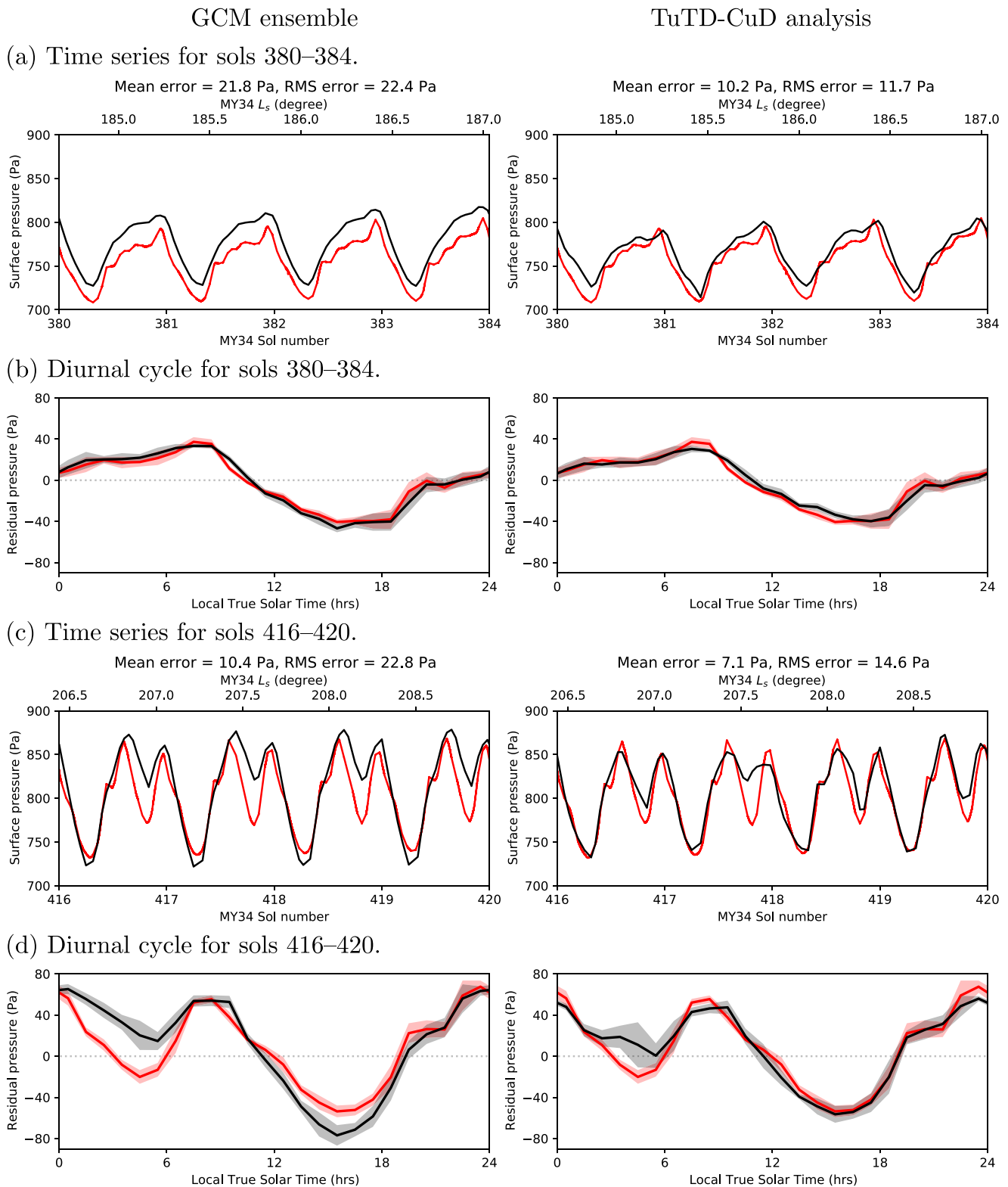


Figure 21.

difficulties associated with interpolating into a crater, is encouraging for possible future assimilation of surface pressure observations.

As the analysis verifies well against Curiosity observations, Figure 22 shows surface pressure diurnal cycles at several other locations; we may reasonably believe the analysis reproduces the surface pressure diurnal cycle there. These points of interest are: the final location of the Opportunity rover (which succumbed to dust loading during the study period); the landing sites for Perseverance and Insight, both currently operational; the Viking 2 landing site, chosen as it is one of the locations used to tune the pressure cycle in the Mars PCM; Acidalia, where flushing dust storms often originate, and within the northern hemisphere baroclinic zone; Hellas, where global dust events have originated (Mulholland et al., 2013), and the location of the highest surface pressures on Mars; and Tharsis, the location of the lowest surface pressures on Mars.

In all cases the surface pressure increases from before the storm to the peak of the storm, ranging from about +20 Pa in Hellas to about +80 Pa at the Viking 2 landing site. The magnitude of the diurnal mode also increases at the peak of the storm, and at most locations the magnitude of the semi-diurnal mode also increases. The day-to-day variability (quantified by the width of the shaded region accompanying each line) is noticeably higher in the analysis than in the GCM ensemble (an equivalent figure to Figure 22 for the GCM ensemble is included as Figure S3 in Supporting Information S1).

The mid-afternoon low at each location is typically weaker in the analysis than in the GCM ensemble, as it was at the Curiosity location, and the mean pressure difference between the analysis and the GCM ensemble is typically 5–15 Pa. One exception is Acidalia (Figure 22e), where the analysis pressure is about 30 Pa higher than the GCM ensemble, and the diurnal cycle is qualitatively different. The diurnal mode is relatively weak compared with other locations, about 20 Pa peak-to-peak before the storm, and 40 Pa at the peak of the storm, and the phase of the diurnal pressure mode is shifted in the analysis by about 3–6 hr relative to the GCM ensemble. Figure 23 shows the pressure time series in both cases for the whole assimilation period. In the GCM ensemble the baroclinic waves are clear, with a period of about eight sols. In the analysis, however, while some signatures of the baroclinic wave remain (peaks at sols 390 and 405, for example), there are shorter-period oscillations that do not appear in the GCM ensemble. Variability on diurnal timescales is also noisier, better reflecting real conditions; we saw this in the Curiosity data set, where the day-to-day variability in the analysis diurnal cycle (Figure 21d, right) is similar to the day-to-day variability in the Curiosity observations.

## 6. Summary and Conclusion

In this paper we have assimilated observations from ACS-TIRVIM, the thermal infrared spectrometer on board ExoMars TGO, into the Mars PCM during the onset and peak of the MY34 GDS. We assimilated both temperature profiles and dust column optical depth measurements using the LETKF in three configurations, with our nominal case TuTD-CuD assimilating temperature profiles to update temperature and dust profiles, followed by CDODs to update the total dust column abundance. We ran an ensemble of Mars PCM simulations alongside the assimilations, constrained by MY34 MCS dust observations. Our other improvement over previous work was to compare forecasts with observations using the retrieval averaging kernels. This allowed a like-by-like comparison to be made between forecast and observation, and by application of a filter to the sum over the averaging kernels at each vertical level, we ensured that information assimilated from the retrievals was strongly weighted toward information from the real atmospheric state rather than the retrieval prior. This is important for assimilating temperature profiles derived from nadir-viewing geometry, which have rather coarse vertical resolution.

Our nominal assimilation verified well against in-sample observations from TIRVIM, and was at least as good as the GCM ensemble when verified against independent MCS observations. We had hoped that our assimilation of ACS observations would be closer to the real Mars atmosphere (as measured by MCS) than the GCM ensemble,

**Figure 21.** Surface pressure time series and diurnal cycle at the Curiosity rover location. The left column shows the Global Climate Model (GCM) ensemble, and the right column shows assimilation TuTD-CuD. In each case the red line shows the Curiosity data, and the black line shows the analysis or GCM ensemble. (a and b) are before the storm, sols 380–384, and (c and d) are at the peak of the storm, sols 416–420. Panels (a and c) show surface pressure time series, corrected for the difference in surface elevation between the GCM grid and the rover location on the surface, but otherwise unmodified. Panels (b and d) show the same data binned into 30-min local true solar time bins, where the mean in each bin is the thick line, and the shaded region shows  $\pm$  the standard deviation. Before binning the data the diurnal mean pressure was removed from the time series using a 1-sol moving average. The mean and RMS surface pressure (analysis/GCM—Curiosity) are listed above each time series.

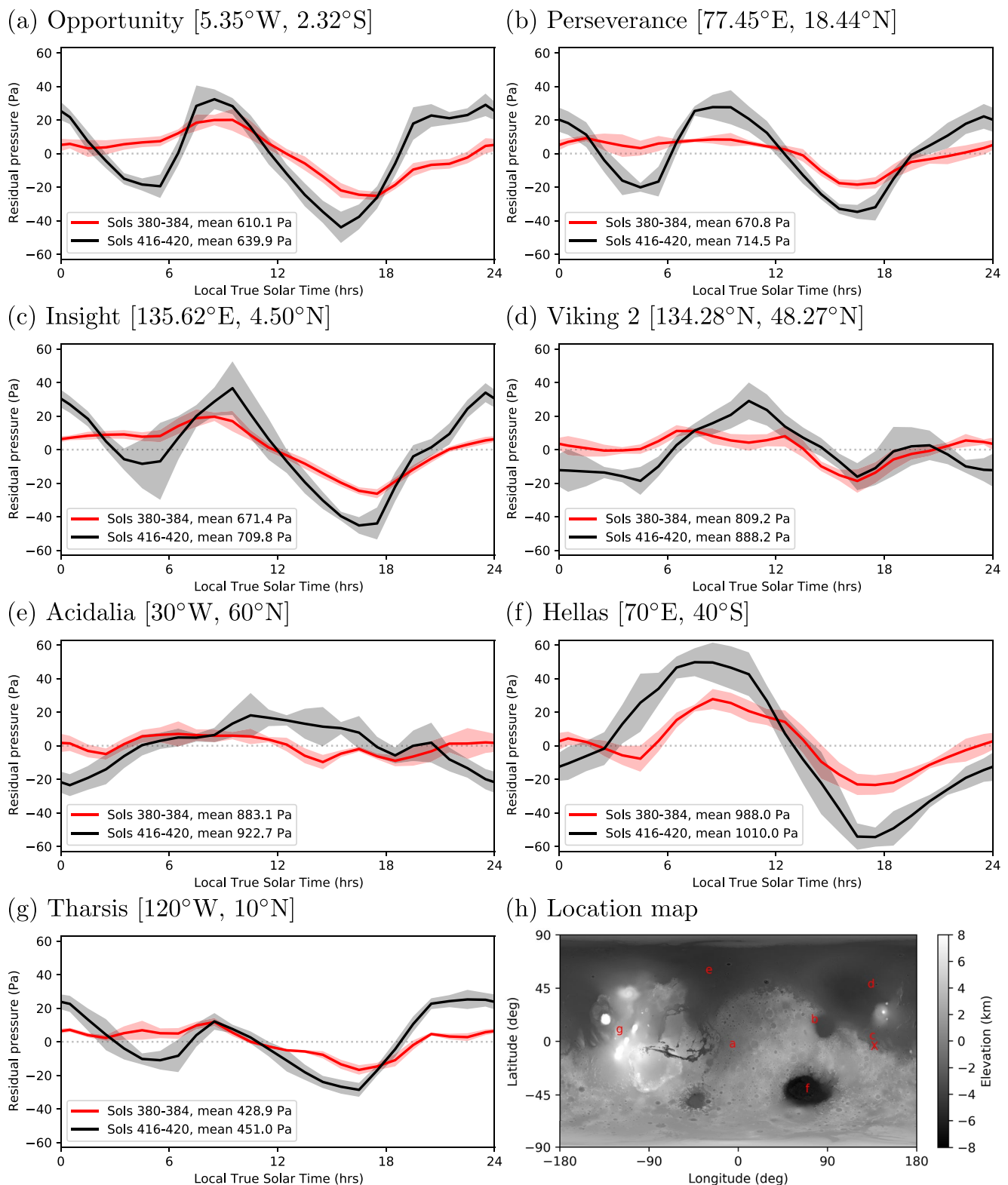


**Figure 22.** Surface pressure diurnal cycles at several locations during assimilation TuTD-CuD. Red lines are from the period before the storm (sols 380–384) and black lines are from the peak of the storm (sols 416–420). The diurnal cycle plots are otherwise the same as in Figure 21. The mean pressure over each 4-sol period is given in each legend. The locations are (a) Opportunity final location; (b) Perseverance landing site; (c) Insight landing site; (d) Viking 2 landing site (these locations were all obtained using NASA GISS' Mars24 software); (e) Acidalia; (f) Hellas; and (g) Tharsis. Panel (h) shows these seven locations with an additional X at the Curiosity landing site, for reference (137.44°E and 4.59°S); topography is from Mars Orbital Laser Altimeter (D. E. Smith et al., 2001).

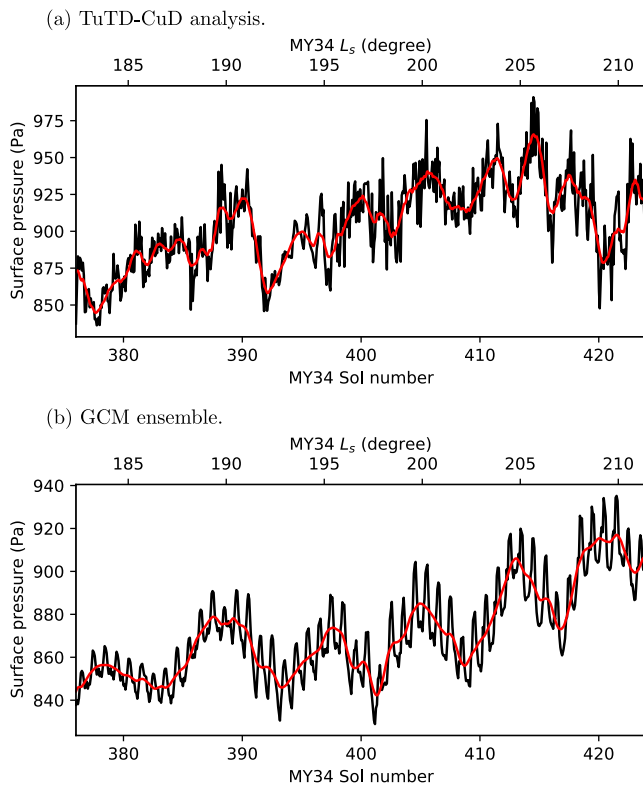


**Figure 23.** Surface pressure time series in Acidalia (30°W and 60°N) throughout the full assimilation period for (a) analysis TuTD-CuD and (b) the Global Climate Model (GCM) ensemble. Black shows the instantaneous surface pressure (every 2 hr) and red shows a running diurnal mean. Note the different y-axis scales.

but this was not generally the case. It is not that discouraging, however, as the GCM ensemble is itself constrained by MCS dust opacities, and we were able to match its performance against MCS by assimilating ACS observations. There was a significant reduction in RMS error when verifying temperatures against MCS once we assimilated CDOD observations, particularly during the growth period of the storm when dust opacities were changing rapidly, so this was encouraging.

The atmospheric temperature structure at 30 Pa followed the MCS observations closely in our TuTD-CuD case, and was noticeably closer to the MCS values than the GCM ensemble (Figures 11c–11e). While the 3 p.m. analysis dust DSO did not reach the maximum observed by MCS at the peak of the storm, there was particularly good correspondence with MCS at 3 a.m. The analysis reproduced detached dust layers, while the GCM ensemble did not, and the latter also overestimated the dust DSO at the storm's peak (Figure 14). The assimilation retrieved the (unobserved) atmospheric wind structure before and during the storm, which showed that the meridional overturning circulation significantly strengthened during the storm (Figure 15), as well as the development of a  $125 \text{ m s}^{-1}$  asymmetry in the midlatitude jets between the two hemispheres (Figure 16).

Assimilating observations over a range of local times gives us confidence in our results related to the diurnal cycle. The diurnal tide strengthened considerably at midlatitudes during the GDS, at the expense of the diurnal tide near the equator (Figure 19), and the semi-diurnal tide increased in strength everywhere, particularly in the lower atmosphere (Figures 17c and 20). The diurnal cycle was also verified against independent Curiosity-REMS surface pressure measurements. Despite the large difference in surface elevation between the GCM topography and the rover, the analysis surface pressures at the peak of the storm accurately reproduced the diurnal cycle measured by Curiosity (Figure 21).

Assimilation during the onset of a Mars GDS is a particularly hard stress test of our assimilation scheme, so it is encouraging that we are able to reproduce

many features of independent observational data sets. But one shortcoming of the assimilation has been made particularly clear when the total amount of dust in the atmosphere changes quickly over time. There is a lag in changes to the global amount of dust (and hence the onset of the GDS) by 6–8 sols (Figure 12c). This is also present in temperature, but it is only 1–2 sols in that case. We expect this is because not all model grid points are updated during each assimilation cycle. If only a small fraction of grid points are updated at any one time, trends in the total amount of dust and heat in the analysis will lag behind such trends in the real atmosphere, because in reality the dust and heat content change at both unobserved and observed locations at the same time. This is a fundamental limitation of the observations, particularly when assimilating data from a single polar-orbiting satellite where the number of model grid columns updated in a single 2-hr assimilation cycle is typically 20%–30% of the total.

This shortcoming could be overcome in a number of ways. First, by simultaneously assimilating more observations at different locations, such as by assimilating MCS in addition to ACS observations. Second, by increasing the length of the assimilation window to include more observations, but this increases the forecast time. Third, by assimilating single observations multiple times, as in AC (Lorenc et al., 1991). Fourth, one could use a longer assimilation window for dust than for temperature. Finally, one could update non-observed locations in some ad hoc way, for example, by assuming that dust lingers in place over some timescale, or by assuming some spatial distribution of dust linking observed locations. This is already done in a sophisticated way for the GCM dust scenarios, which are complete maps but which use incomplete observations with gaps filled in by kriging (Montabone et al., 2015). Only the first of these options avoids some ad hoc intervention or a substantial change to the assimilation method, so the next step will be to focus on joint assimilation of multiple instruments' observations.

## Data Availability Statement

Data sets related to this article can be found on the Figshare online open access repository (Young et al., 2022). The processed TIRVIM data and retrievals used in this paper are available in NetCDF format on the Institut Pierre Simon Laplace (IPSL) data server (Guerlet, 2021). The observations use version seven of the retrieval algorithm, and version four of the IKI calibration algorithm. Mars Climate Sounder observations are available on the NASA Planetary Data System Atmospheres node at [https://pds-atmospheres.nmsu.edu/data\\_and\\_services/atmospheres\\_data/MARS/mars\\_reconnaissance\\_orbiter.html](https://pds-atmospheres.nmsu.edu/data_and_services/atmospheres_data/MARS/mars_reconnaissance_orbiter.html). Mars Science Laboratory Curiosity rover Rover Environmental Monitoring Station observations are available on the NASA Planetary Data System Atmospheres node at [https://atmos.nmsu.edu/data\\_and\\_services/atmospheres\\_data/MARS/curiosity/rem\\_s.html](https://atmos.nmsu.edu/data_and_services/atmospheres_data/MARS/curiosity/rem_s.html). MOLA topography data are available on the NASA Planetary Data System Geosciences node (Smith et al., 2003). The Mars PCM is available from <http://www-mars.lmd.jussieu.fr/>; we used subversion revision r2533. The assimilation uses letkfmars git revision f28935f6472a280394a98ac64f99213d1cbb2e01. Mars24 is available from the NASA GISS at <https://www.giss.nasa.gov/tools/mars24/>.

## Acknowledgments

ExoMars is a space mission of ESA and Roscosmos. The Atmospheric Chemistry Suite (ACS) experiment is led by IKI, the Space Research Institute in Moscow, Russia, assisted by LATMOS in France. This work, exploiting ACS/TIRVIM data, acknowledges funding by the CNES. The science operations of ACS are funded by Roscosmos and ESA. The ACS/TIRVIM team at IKI acknowledges the subsidy of the Ministry of Science and Higher Education of Russia. The authors acknowledge Sandrine Guerlet and the ACS/TGO team for supplying the data and the data center ESPRI/IPSL for their help in accessing the data. R. M. B. Young acknowledges funding from the UAE University grants G00003322 and G00003407. Supercomputing resources were provided by the UAE University High Performance Computing, with technical support from Anil Thomas and Asma Alneyadi, and at LMD by the IPSL mesocentre. The authors thank Luca Montabone for access to processed versions of Mars Climate Sounder temperature and dust observations, and Thomas Navarro and Claus Gebhardt for useful discussions.

## References

- Ahn, S., & Fessler, J. A. (2003). *Standard errors of mean, variance, and standard deviation estimators* (Technical Report 413). Communications and Signal Processing Laboratory, Department of EECS, University of Michigan.
- Amiri, S., Brain, D., Sharaf, O., Withnell, P., McGrath, M., Alloghani, M., et al. (2022). The Emirates Mars mission. *Space Science Reviews*, 218(1), 4. <https://doi.org/10.1007/s11214-021-00868-x>
- Barnes, J. R., Haberle, R. M., Wilson, R. J., Lewis, S. R., Murphy, J. R., & Read, P. L. (2017). The global circulation. In *The atmosphere and climate of Mars* (pp. 229–294). Cambridge University Press.
- Capderou, M., & Forget, F. (2004). Optimal orbits for Mars atmosphere remote sensing. *Planetary and Space Science*, 52(9), 789–798. <https://doi.org/10.1016/j.pss.2004.03.006>
- Evensen, G. (2003). The Ensemble Kalman Filter: Theoretical formulation and practical implementation. *Ocean Dynamics*, 53(4), 343–367. <https://doi.org/10.1007/s10236-003-0036-9>
- Forget, F., Hourdin, F., Fournier, R., Hourdin, C., Talagrand, O., Collins, M., et al. (1999). Improved general circulation models of the Martian atmosphere from the surface to above 80 km. *Journal of Geophysical Research: Planets*, 104(E10), 24155–24175. <https://doi.org/10.1029/1999JE001025>
- Forget, F., Millour, E., Vals, M., Zakharov, V., & Lewis, S. R. (2017). Mars Climate Database v5.3 Detailed Design Document. In *Laboratoire de Météorologie Dynamique* (Technical Report). Retrieved from [http://www-mars.lmd.jussieu.fr/mars/info\\_web/MCD5.3\\_ddd.pdf](http://www-mars.lmd.jussieu.fr/mars/info_web/MCD5.3_ddd.pdf)
- Francois, F., Millour, E., Bierjon, A., Delavois, A., Fan, S., Lange, L., et al. (2022). Challenges in Mars Climate Modelling with the LMD Mars Global Climate Model, Now Called the Mars “Planetary Climate Model” (PCM). In *Seventh international workshop on the Mars atmosphere: Modelling and observations*. Retrieved from [http://www-mars.lmd.jussieu.fr/paris2022/abstracts/oral\\_Forget\\_Francois.pdf](http://www-mars.lmd.jussieu.fr/paris2022/abstracts/oral_Forget_Francois.pdf)
- Giuranna, M., Wolkenberg, P., Grassi, D., Aronica, A., Aoki, S., Scaccabarozzi, D., et al. (2021). The current weather and climate of Mars: 12 years of atmospheric monitoring by the Planetary Fourier Spectrometer on Mars Express. *Icarus*, 353, 113406. <https://doi.org/10.1016/j.icarus.2019.113406>
- Greybush, S. J., Wilson, R. J., Hoffman, R. N., Hoffman, M. J., Miyoshi, T., Ide, K., et al. (2012). Ensemble Kalman Filter data assimilation of Thermal Emission Spectrometer temperature retrievals into a Mars GCM. *Journal of Geophysical Research: Planets*, 117(E11), E11008. <https://doi.org/10.1029/2012JE004097>
- Guerlet, S. (2021). ACS/TIRVIM temperature and aerosol retrievals [Data set]. ESPRI/IPSL. <https://doi.org/10.14768/AB765EBA-0C1D-47B6-97D6-6390C63F0197>
- Guerlet, S., Ignatiev, N., Forget, F., Fouchet, T., Vlasov, P., Bergeron, G., et al. (2022). Thermal structure and aerosols in Mars’ atmosphere from TIRVIM/ACS onboard the ExoMars Trace Gas Orbiter: Validation of the retrieval algorithm. *Journal of Geophysical Research: Planets*, 127(2), e2021JE007062. <https://doi.org/10.1029/2021JE007062>
- Hamill, T. M., Whitaker, J. S., & Snyder, C. (2001). Distance-dependent filtering of background error covariance estimates in an Ensemble Kalman Filter. *Monthly Weather Review*, 129(11), 2776–2790. [https://doi.org/10.1175/1520-0493\(2001\)129<2776:DDFOBE>2.0.CO;2](https://doi.org/10.1175/1520-0493(2001)129<2776:DDFOBE>2.0.CO;2)
- Heavens, N. G., Richardson, M. I., Kleinböhl, A., Kass, D. M., McCleese, D. J., Abdou, W., et al. (2011). Vertical distribution of dust in the Martian atmosphere during northern spring and summer: High-altitude tropical dust maximum at northern summer solstice. *Journal of Geophysical Research: Planets*, 116(E1), E01007. <https://doi.org/10.1029/2010JE003692>
- Hersbach, H., Bell, W., Berrisford, P., Horányi, A., Sabater, J. M., Nicolas, J., et al. (2019). Global reanalysis: Goodbye ERA-Interim, hello ERA5. *ECMWF Newsletter*, 159, 17–24. <https://doi.org/10.21957/vf291hehd7>
- Hoffman, M. J., Greybush, S. J., Wilson, R. J., Gyarmati, G., Hoffman, R. N., Kalnay, E., et al. (2010). An Ensemble Kalman Filter data assimilation system for the Martian atmosphere: Implementation and simulation experiments. *Icarus*, 209(2), 470–481. <https://doi.org/10.1016/j.icarus.2010.03.034>
- Hoffman, R. N. (2011). A retrieval strategy for interactive ensemble data assimilation. *arXiv:1009.1561*.
- Holmes, J. A., Lewis, S. R., Patel, M. R., & Lefèvre, F. (2018). A reanalysis of ozone on Mars from assimilation of SPICAM observations. *Icarus*, 302, 308–318. <https://doi.org/10.1016/j.icarus.2017.11.026>
- Holmes, J. A., Lewis, S. R., Patel, M. R., & Smith, M. D. (2019). Global analysis and forecasts of carbon monoxide on Mars. *Icarus*, 328, 232–245. <https://doi.org/10.1016/j.icarus.2019.03.016>
- Hunt, B. R., Kostelich, E. J., & Szunyogh, I. (2007). Efficient data assimilation for spatiotemporal chaos: A local ensemble transform Kalman filter. *Physica D*, 230(1–2), 112–126. <https://doi.org/10.1016/j.physd.2006.11.008>
- Kahre, M. A., Murphy, J. R., Newman, C. E., Wilson, R. J., Cantor, B. A., Lemmon, M. T., & Wolff, M. J. (2017). The Mars dust cycle. In *The atmosphere and climate of Mars* (pp. 295–337). Cambridge University Press.
- Kalnay, E. (2003). *Atmospheric modeling, data assimilation and predictability*. Cambridge University Press.

- Kass, D. M., Schofield, J. T., Kleinböhl, A., McCleese, D. J., Heavens, N. G., Shirley, J. H., & Steele, L. J. (2019). Mars Climate Sounder observation of Mars' 2018 global dust storm. *Geophysical Research Letters*, *46*(23), e2019GL083931. <https://doi.org/10.1029/2019GL083931>
- Kleinböhl, A., Schofield, J. T., Kass, D. M., Abdou, W. A., Backus, C. R., Sen, B., et al. (2009). Mars Climate Sounder limb profile retrieval of atmospheric temperature, pressure, and dust and water ice opacity. *Journal of Geophysical Research: Planets*, *114*(E10), E10006. <https://doi.org/10.1029/2009JE003358>
- Kleinböhl, A., Spiga, A., Kass, D. M., Shirley, J. H., Millour, E., Montabone, L., & Forget, F. (2020). Diurnal variations of dust during the 2018 global dust storm observed by the Mars Climate Sounder. *Journal of Geophysical Research: Planets*, *125*(1), e2019JE006115. <https://doi.org/10.1029/2019JE006115>
- Kleinböhl, A., Wilson, R. J., Kass, D., Schofield, J. T., & McCleese, D. J. (2013). The semidiurnal tide in the middle atmosphere of Mars. *Geophysical Research Letters*, *40*(10), 1952–1959. <https://doi.org/10.1002/grl.50497>
- Korablev, O., Montmessin, F., Trokhimovskiy, A., Fedorova, A. A., Shakun, A. V., Grigoriev, A. V., et al. (2018). The Atmospheric Chemistry Suite (ACS) of three spectrometers for the ExoMars 2016 Trace Gas Orbiter. *Space Science Reviews*, *214*(1), 7. <https://doi.org/10.1007/s11214-017-0437-6>
- Lee, C., Lawson, W. G., Richardson, M. I., Anderson, J. L., Collins, N., Hoar, T., & Mischna, M. (2011). Demonstration of ensemble data assimilation for Mars using DART, MarsWRF, and radiance observations from MGS TES. *Journal of Geophysical Research: Planets*, *116*(E11), E11011. <https://doi.org/10.1029/2011JE003815>
- Lewis, S. R., & Barker, P. R. (2005). Atmospheric tides in a Mars general circulation model with data assimilation. *Advances in Space Research*, *36*(11), 2162–2168. <https://doi.org/10.1016/j.asr.2005.05.122>
- Lewis, S. R., & Read, P. L. (1995). An operational data assimilation scheme for the Martian atmosphere. *Advances in Space Research*, *16*(6), 9–13. [https://doi.org/10.1016/0273-1177\(95\)00244-9](https://doi.org/10.1016/0273-1177(95)00244-9)
- Lewis, S. R., Read, P. L., Conrath, B. J., Pearl, J. C., & Smith, M. D. (2007). Assimilation of thermal emission spectrometer atmospheric data during the Mars Global Surveyor aerobraking period. *Icarus*, *192*(2), 327–347. <https://doi.org/10.1016/j.icarus.2007.08.009>
- Lorenç, A. C., Bell, R. S., & Macpherson, B. (1991). The Meteorological Office analysis correction data assimilation scheme. *Quarterly Journal of the Royal Meteorological Society*, *117*(497), 59–89. <https://doi.org/10.1002/qj.49711749704>
- Madeleine, J.-B., Forget, F., Millour, E., Montabone, L., & Wolff, M. J. (2011). Revisiting the radiative impact of dust on Mars using the LMD Global Climate Model. *Journal of Geophysical Research: Planets*, *116*(E11), E11010. <https://doi.org/10.1029/2011JE003855>
- Montabone, L., Forget, F., Millour, E., Wilson, R. J., Lewis, S. R., Cantor, B., et al. (2015). Eight-year climatology of dust optical depth on Mars. *Icarus*, *251*, 65–95. <https://doi.org/10.1016/j.icarus.2014.12.034>
- Montabone, L., Marsh, K., Lewis, S. R., Read, P. L., Smith, M. D., Holmes, J., et al. (2014). The Mars analysis correction data assimilation (MACDA) dataset V1.0. *Geoscience Data Journal*, *1*(2), 129–139. <https://doi.org/10.1002/gdj3.13>
- Montabone, L., Spiga, A., Kass, D. M., Kleinböhl, A., Forget, F., & Millour, E. (2020). Martian year 34 column dust climatology from Mars Climate Sounder observations: Reconstructed maps and model simulations. *Journal of Geophysical Research: Planets*, *125*(8), e2019JE006111. <https://doi.org/10.1029/2019JE006111>
- Mulholland, D. P., Read, P. L., & Lewis, S. R. (2013). Simulating the interannual variability of major dust storms on Mars using variable lifting thresholds. *Icarus*, *223*(1), 344–358. <https://doi.org/10.1016/j.icarus.2012.12.003>
- Navarro, T., Forget, F., Millour, E., & Greybush, S. J. (2014). Detection of detached dust layers in the Martian atmosphere from their thermal signature using assimilation. *Geophysical Research Letters*, *41*(19), 6620–6626. <https://doi.org/10.1002/2014GL061377>
- Navarro, T., Forget, F., Millour, E., Greybush, S. J., Kalnay, E., & Miyoshi, T. (2017). The challenge of atmospheric data assimilation on Mars. *Earth and Space Science*, *4*(12), 690–722. <https://doi.org/10.1002/2017EA000274>
- Pottier, A., Forget, F., Montmessin, F., Navarro, T., Spiga, A., Millour, E., et al. (2017). Unraveling the Martian water cycle with high-resolution global climate simulations. *Icarus*, *291*, 82–106. <https://doi.org/10.1016/j.icarus.2017.02.016>
- Rafkin, S. C. R., Spiga, A., & Michaels, T. I. (2017). Mesoscale meteorology. In *The atmosphere and climate of Mars* (pp. 203–228). Cambridge University Press.
- Rodgers, C. D., & Connor, B. J. (2003). Intercomparison of remote sounding instruments. *Journal of Geophysical Research: Atmospheres*, *108*(D3), 4116. <https://doi.org/10.1029/2002JD002299>
- Ruan, T., Young, R. M. B., Lewis, S. R., Montabone, L., Valeanu, A., & Read, P. L. (2021). Assimilation of both column- and layer-integrated dust opacity observations in the Martian atmosphere. *Earth and Space Science*, *8*(12), e2021EA001869. <https://doi.org/10.1029/2021EA001869>
- Smith, D. E., Zuber, M. T., Frey, H. V., Garvin, J. B., Head, J. W., Muhleman, D. O., et al. (2001). Mars Orbiter Laser Altimeter: Experiment summary after the first year of global mapping of Mars. *Journal of Geophysical Research: Planets*, *106*(E10), 23689–23722. <https://doi.org/10.1029/2000JE001364>
- Smith, D. E., Zuber, M. T., Neumann, G. A., Guinness, E. A., & Slavney, S. (2003). Mars Global Surveyor Laser Altimeter Mission Experiment Gridded Data Record [Data set]. NASA Planetary Data System, MGSM-MOLA-5-MEGDR-L3-V1.0. <https://doi.org/10.17189/1519460>
- Smith, M. D., Bougher, S. W., Encrenaz, T., Forget, F., & Kleinböhl, A. (2017). Thermal structure and composition. In *The atmosphere and climate of Mars* (pp. 42–75). Cambridge University Press.
- Spiga, A., Forget, F., Dolla, B., Vinatier, S., Melchiorri, R., Drossart, P., et al. (2007). Remote sensing of surface pressure on Mars with the Mars Express/OMEGA spectrometer: 2. Meteorological maps. *Journal of Geophysical Research: Planets*, *112*(E8), E08S16. <https://doi.org/10.1029/2006JE002870>
- Steele, L. J., Lewis, S. R., & Patel, M. R. (2014). The radiative impact of water ice clouds from a reanalysis of Mars Climate Sounder data. *Geophysical Research Letters*, *41*(13), 4471–4478. <https://doi.org/10.1002/2014GL060235>
- Steele, L. J., Lewis, S. R., Patel, M. R., Montmessin, F., Forget, F., & Smith, M. D. (2014). The seasonal cycle of water vapour on Mars from assimilation of Thermal Emission Spectrometer data. *Icarus*, *237*, 97–115. <https://doi.org/10.1016/j.icarus.2014.04.017>
- Young, R. M. B., Millour, E., Guerlet, S., Forget, F., Ignatiev, N., Grigoriev, A. V., et al. (2022). Mars atmosphere reanalyses during the MY34 Global Dust Storm produced by assimilation of ExoMars TGO-ACS-TIRVIM observations into the Mars PCM using the LETKF [Data set]. Figshare. <https://doi.org/10.6084/m9.figshare.20709451.v1>